

Smart Memory Cast

A new approach for cast treatment in distal radius fractures

Thesis paper

by

Aurelie Soors

to obtain the degree of Master of Science
at the Delft University of Technology
to be defended publicly on March 24, 2023 at 13:30

Thesis committee:

Chair: Dr. A. Hunt
Supervisors: Dr. A. Hunt, TU Delft
Dr. S. Janbaz, UvA
Dr. J. Colaris, Erasmus UMC
External examiner: Dr.ir. T. Horeman
Place: Faculty of 3mE, Delft
Student number: 4462491

Smart Memory Cast: a new approach for cast treatment in distal radius fractures

AURELIE SOORS (4462491)¹

¹Master: Biomedical Engineering, Thesis paper, Delft University of Technology, The Netherlands.

In up to 39% of reduced distal radius fractures, re-displacement of the fracture occurs in the cast. In most cases, the cast becomes too loose as soft tissue swelling decreases over time and the cast no longer provides sufficient support to keep the fracture reduced. This issue could be addressed by introducing a smart memory cast, a cast that would employ soft polymer foam to relieve stress concentration while providing the required support stiffness to maintain the reduction throughout the whole cast treatment period. Soft polymer foams are characterised by a plateau phase in which the pressure does not increase as the material is compressed. The concept is tested by placing a soft polyurethane foam between an artificial arm that mimics soft tissue swelling and a synthetic cast. The pressure in the smart memory cast is measured by thin film pressure sensors. The average pressure in the smart memory cast was 15.4 mmHg and was reduced by 47.8% compared to the average pressure measured, 29.5 mmHg, in a traditional cast. The pressure in the smart memory cast remained under 25.0 mmHg which was set as a threshold value that could lead to a compartment syndrome. In contrast with the traditional cast where the pressure kept increasing above the threshold value as the artificial arm kept swelling, in the smart memory cast the pressure plateaued. The results from this study show that by introducing a filler material with non-linear elastic properties in a synthetic cast, the pressure concentration is reduced compared to a traditional cast and the pressure plateaus as soft tissue swelling increases.

Keywords: *Cast Treatment, Distal Radius Fracture, Forearm Fracture, Smart Memory Cast*

1. INTRODUCTION

Distal radius fractures (DRFs) are one of the common injuries seen in the Emergency Room (ER). According to different epidemiology and incidence studies, children, young adolescents and the elderly are at a higher risk for this type of fracture [1–4]. In children and young adolescents, the main causes of DRF are playing and physical activities. While in the elderly it is due to low-trauma fall from standing height position [1, 5–7]. Over the past few years, the incidence of DRF has further increased worldwide due to a longer life expectancy in the elderly and children participating in more sports activities [1–4, 8, 9]. Most DRFs are displaced and therefore need to

be reduced and a rigid cast is applied to immobilize the fracture to prevent re-displacement of the fracture [9–12].

However, re-displacement of the fracture occurs up to 39% which often results in surgical stabilisation of the fracture [13–16]. Many different factors, (fracture-, patient- and lastly treatment-related) can be responsible for the re-displacement. Factors related to the fracture and patient are not changeable, however, the treatment factors can be mitigated. The quality of the cast is an important factor [16, 17]. If the quality is low, the cast does not provide sufficient support to keep the reduced fracture in position which can result in re-displacement of the

fracture. The quality of the cast mould can be verified by the radiographic indices: cast index and three-point index. These indices are measured after the cast is applied and are correlated with the risk for re-displacement [18, 19].

Post-traumatic soft tissue swelling occurs in the area around the bone fracture as a response to the initial inflammatory phase and proceeds for several days. This means that the soft tissue continues to swell after the rigid cast is applied. Due to this the intracompartmental pressure inside the fractured forearm increases and this could lead in severe cases to a compartment syndrome (CS), soft tissue necrosis and even amputation as the blood flow to the soft tissue is restricted [20–22]. To accommodate this swelling, a univalve or bivalve cut can be made along the length of the cast. To further decrease the intracompartmental pressure, a cast spacer can be placed in between the cut. However, a drawback of this method is that once the swelling has decreased, the cast becomes too loose and no longer provides sufficient support to keep the fracture reduced and thus re-displacement can occur. Thereby, the patient has to revisit the hospital to get a new cast [23–26].

A solution to this problem could be the introduction of a new type of cast, smart memory cast (SMC). This cast can adapt itself to the degree of soft tissue swelling around the fracture site without increasing the intracompartmental pressure while providing enough support to keep the reduction in place. This can be done by positioning a filler material between the synthetic cast and the forearm (Figure 1). As soft tissue swelling decreases the cast is still able to provide enough support to keep the fracture reduced as the filler material adjusts itself. In this paper, a prototype of such a smart memory cast will be developed and tested. This is done by first establishing the material properties needed and which materials can provide these. An artificial arm is manufactured to mimic soft tissue swelling after a fracture and the smart memory cast is assembled such that experiments can be

carried out. All this information can be found in section 2. Next, the results from the experiments are shown and discussed in section 3. Finally, in section 4, a conclusion is drawn.

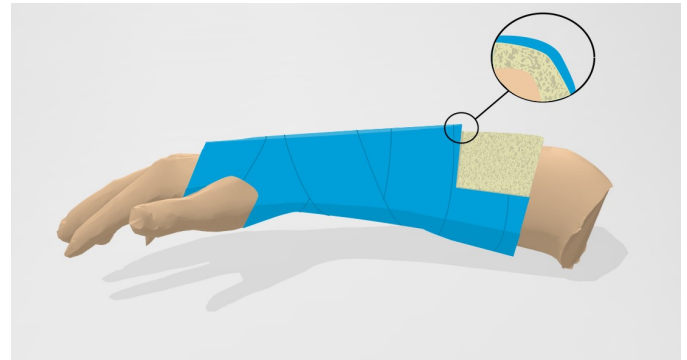


Fig. 1. A pictorial diagram of the smart memory cast. From the inside to the outside: the forearm, the filler material and lastly the rigid cast.

2. MATERIALS AND METHODOLOGY

Before the new adaptable cast can be tested, a filler material with the desired material properties has to be chosen that will be placed between the cast and the arm. The required pressure to maintain a reduction is obtained from literature. Based on these findings and the needed non-linear elastic material properties, possible filler materials are selected. These materials are then subjected to a quasi-static compression test so that a final material can be chosen. To test the new adaptable cast, an artificial arm will be manufactured that can mimic soft tissue swelling that occurs after a bone fracture. The pressure in the smart memory cast is measured by thin film pressure sensors. The filler material and the artificial arm were wrapped with synthetic cast material to achieve the smart memory cast. Lastly, the pressure sensors were installed and the artificial arm was connected to a syringe pump such that smart memory cast could be tested. All the aspects of developing and testing the smart memory cast are explained in more detail in the following sections.

A. Filler Material Requirements

Little research has been done about how much the intracast pressure should be to maintain a reduction [27–30]. Therefore, in an experiment performed at Erasmus University Medical Center (UMC), sensors were placed on the forearm such that the pressure could be measured during the application process of a traditional cast (TC) and once it was completely cured. From the results, it was found that the cast should apply around 2652.1 ± 93.2 Pa (mean \pm SD) or 19.90 ± 0.70 mmHg on the skin such that the fracture maintains reduced which corresponds with values found in literature. More information about the experiment can be found in appendix B.

An important criterion of the filler material is that it can adjust to swelling keeping a constant pressure on the forearm while maintaining the fracture reduction throughout the cast treatment period, without causing skin irritation or CS. If the cast is too tight, the pressure increases on the skin. This increased pressure reduces the capillary perfusion in the skin which could lead to pressure sores [24, 31]. If no action is taken, this could lead to tissue necrosis and in the worst case amputation [24, 29, 32]. Therefore, the pressure in the cast may not exceed 30 mmHg. For safety purposes, the maximum pressure in the cast may not surpass 25 mmHg [29, 33–35].

The filler material should be able to adjust to the degree of soft tissue swelling without increasing the pressure on the forearm. This indicates that the filler material should have some non-linear elastic properties, such that as the strain increases the pressure on the material does not and remains constant. This corresponds with a plateau phase in the stress-strain curve of the material. In the research done by A. Younger et al. [30], it was seen that the circumference of a fractured wrist is 2.1 cm larger compared to a non-fractured wrist. After the wrist fracture is reduced, the circumference can further increase by 5 mm. If the shape of the wrist is assumed to approximate a circle, the radius increases by

4.3 mm during swelling. To accommodate for this swelling, the thickness of the soft polymer foam layer should be 20 mm such that the operating range stays within the range of the plateau phase.

B. Filler Material Selection

The filler material should provide constant pressure as soft tissue swelling fluctuates during treatment. So, the pressure should remain constant as the strain increases and decreases on the material. Polymer foam has a non-linear elastic behaviour that is characterised by three distinct phases as the strain increases: a linear elastic phase followed by a plateau phase and a densification phase [36]. In this plateau phase, as the strain increases the pressure plateaus as can be seen in figure 2. In this phase, the cell walls buckle and collapse and the energy is absorbed and distributed by the foam. Therefore, polymer foams can be used as a filler material as long as their operating range is within the plateau phase [37, 38]. Further, the average pressure during this plateau phase should correspond with the pressure needed to maintain the reduction.

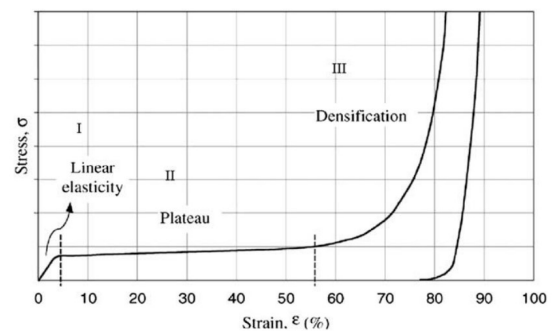


Fig. 2. General stress-strain curve of foam materials under uniaxial compression [36].

The stiffness of the polymer foam is mainly affected by its relative density. The lower the relative density is, the lower the elastic modulus is. Thus, different polymer foams with low relative densities were tested. Three different types of polyether (PE 25, 35, 40) foam with relative densities of 25, 30 and 40 kg/m³, a polyurethane (PU 40) with a relative density of 40 kg/m³ and one memory foam (MF) were tested.

C. Quasi-Static Compression Test

A quasi-static compression test (*Instron 6800 series*) was performed on the polymer foams such that the stress-strain curve could be obtained for each foam sample. The stress-strain curve provides information about the material properties of the foam such as its stiffness, the length of the plateau phase, and the average pressure of the plateau phase. The different polymer foams were cut into cubes with dimensions of 50x50x50 mm. The applied loading rate was 0.1 mm/s and continued until the sample was compressed to 80% of its original height. From each foam type, three samples were made and tested. The test setup can be seen in figure 3. From the test, the force and displacement were obtained which were then converted to stress and strain such that the stress-strain curve of each sample can be plotted.

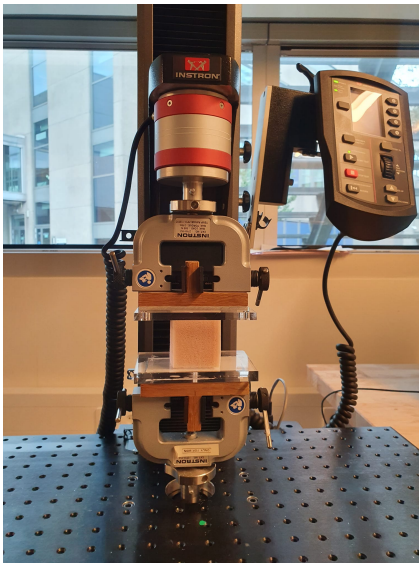


Fig. 3. The quasi-static compression machine with a PE35 foam sample is placed in alignment with the centre of the machine.

D. Artificial Arm

An artificial arm is designed and constructed in order to study the effects of swelling in the presence of the traditional and smart memory cast concepts.

A 3D model of a forearm is divided into six

individual segments. On each segment, alterations are made such that a silicone tube can be connected to it, a silicone band can be attached to it and the segments can be assembled back into a forearm. From the inlet on the inside of the segment, a pipe is made from the inlet to the outer surface of that segment so water from the inlet can flow through it. Each segment is covered with a silicone band that is able to expand when water is pushed through a silicone tube attached to the inlet of that segment. This expansion mimics soft tissue swelling. Water can also be withdrawn from the segment such that it converts back to its original size.

In the CAD software SolidWorks, first, the moulds for the silicone bands for each segment are made. Next, alterations such as adding an inlet, brims and a straight hole through the segment are done to the individual segments. The moulds and segments are 3D printed (*Original Prusa i3 MK3S+*) from PLA. The silicone bands are made by mixing equal parts of A and B of *ecoflexTM 00-50* and pouring it into the mould. The mixture is degassed using a vacuum pump and left to cure for three hours. The silicone band is sealed in place to its corresponding segment. To each inlet, a silicone tube is connected. The individual parts are assembled on a straight steel rod back into the shape of a forearm while all the silicone tubes come out of the proximal side of the forearm. Lastly, to prevent water leakage, the hollow inside of the arm is filled with *ecoflexTM 00-30*. The final assembled artificial arm can be seen in figure 4. A more detailed explanation of the manufacturing process of the artificial arm can be found in appendix C.

E. Pressure Sensing in Cast

The pressure between the cast and the artificial arm is measured by thin film pressure sensors. In total six pressure sensors are used. They are positioned such that the pressure in the cast in the proximity of a DRF can be measured. Two sensors are placed on the hand, the wrist and the first arm part. One sensor is placed on the anterior side (bottom) of the forearm and the



Fig. 4. The artificial arm is made of individual 3D-printed PLA segments covered with a silicone band combined on a steel rod.

other on the posterior side (top) of the forearm.

Two different types of thin film pressure sensors, (*SEN0295, DRFRobot, Shanghai, China* and *406 FSR, Interlink Electronics, Camarillo, California, USA*), are tested since the polymer foam layer influences the sensitivity of the sensor. Each sensor that is tested, twelve SEN0295 and four 406FSR sensors, is placed in series with a resistor of 10 k Ω . The sensor receives an input voltage of 5 V from a DAQ system (*National InstrumentsTM*). With this voltage divider circuit, the voltage output can be collected through the DAQ system at a sample rate of 10 Hz. Further, 2 mm thick PMMA plates with the same dimensions as the sensors are placed on the sides of sensors such that the sensor readings will not be influenced by bending.

The sensors are calibrated by performing a compression test with the polymer foam chosen. In the SMC the polymer foam layer has a required thickness of 20 mm, therefore, the polymer foam used during the calibration process also has a thickness of 20 mm. The sensor is placed under the polymer foam layer during the compression test. The strain rate is again 0.1 mm/s and the foam is compressed up until 80%. While the compression test is running, the sensor is simultaneously running and the data is collected by the DAQ system. The data from the sensors and

the compression test are then synchronised. The period of the operating range of the sensors is obtained from the data. The period is then transferred to the compression test data such that the stress range and sensitivity range, of the sensors is acquired. This stress range is plotted over the stress-strain curve of the polymer foam to see if the stress range includes the plateau phase. From these results, the sensors are chosen that are used in the final experiment setup. Further, the sensors are calibrated by plotting the voltage measured against the stress measured during the compression test.

F. Smart Memory Cast

In the SMC, the cotton layer that is used as padding in TC is replaced with a soft polymer foam layer with a thickness of 20 mm. The polymer foam layer is covered with the same synthetic cast material used in a traditional cast, a visual example can be seen in figure 1.

To test the new SMC, a removable cast is made by a casting technician (CT) at Erasmus UMC Rotterdam. The artificial arm is wrapped with the soft polymer layer beforehand. The CT wraps Delta-cast[®] conformable, a non-fibreglass casting tape with an elastic, knitted polyester substrate, that is dipped in room temperature water around the artificial arm with 50% overlap. During the curing phase of the material, the cast is moulded around the artificial arm with the palm of the hands by the CT. Next, a cast saw is used to cut the cast open such that it could be removed from the artificial arm. Velcro straps are added to the cast such that the cast can be wrapped and closed again around the artificial arm for testing. Afterwards, holes are made in the cast such that the pressure can be measured in the area surrounding a DRF with the sensors. The sensors are held in place by screws and a 3D-printed PLA plate. Finally, the polymer foam material chosen from the compression test is placed in the cast and SMC is complete.

For comparison, a TC is made that is used in clinical practice at Erasmus MC Rotterdam

by the CT. In the TC, the artificial arm is first covered with a stockinette and followed by a cotton layer that has 50% overlap each time the cotton roll was wrapped around the arm. Just as in the SMC, a cast saw is used to remove the cast and velcro straps are added. Holes, in corresponding places as in the SMC, are made in the TC for the sensors.

G. Experimental Validation

For experimentally studying the behaviour of the SMC and compared to the TC, the test setup and procedure is for both casts the same. For the SMC, the artificial arm is placed in the SMC. The sensors are placed in the holes in the cast and connected to a DAQ system. The data is collected on a laptop. The silicone tubes from the artificial arm are connected to a syringe with a valve and a small silicone tube. The syringe is placed in a syringe pump. The final test setup can be seen in figure 5. The same setup is used for the TC but the SMC is changed to a TC.

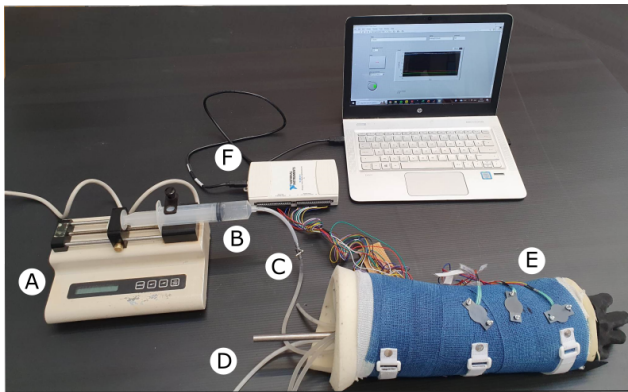


Fig. 5. The experimental setup with the artificial arm and sensors. The syringe (B) is placed in the syringe pump (A). Silicone tubes of the artificial arm (D) are connected to the syringe (B) via a valve and a small silicone tube (C). On the smart memory cast, the pressure sensors are placed (E) and connected to the DAQ system (F). The data is shown and stored on a laptop.

As mentioned earlier, the circumference of a fractured wrist can increase by 2.6 cm compared to

a non-fractured wrist [30]. Therefore, the circumference of the parts from the artificial arm that will be inflated is measured while they are filled with water such that the amount of water needed to get to this increase can be found. The hand, wrist and forearm part have to be filled with 49 ml, 29 ml and 40 ml respectively.

The air is removed from the parts and replaced with water such that it does not influence the pressure readings. The syringe from the hand of the artificial arm in the SMC is placed in the syringe pump and filled with 49 ml of water. The valve is opened and the pump pushes water into the segment at a rate of 0.1 ml/s at the same time the sensors are running mimicking soft tissue swelling. Once the syringe is empty, the valve is closed for 5 minutes. Afterwards, the syringe pump is started again and the valve is opened such that the water can be extracted from the hand, simulating the decrease in soft tissue swelling after a few days during the fracture treatment. After all the water is removed, the sensors will keep running for 5 more minutes. This procedure is repeated for the wrist and arm part with their respective volumes of water. Next, the TC was tested following the same steps.

Further, each segment is injected with water five times repeatedly so that the average pressure can be for each segment in the SMC and TC at the end of the filling phase, when the degree of swelling is the largest, can be determined.

3. RESULTS AND DISCUSSION

A. Polymer Foam Compression Test

In the PE25 foam, the plateau phase was initiated at an average pressure of 3981.5 ± 481.5 Pa and strain of $7.7 \pm 0.1\%$ and ended at 5302 ± 650.5 Pa and $49.6 \pm 0.4\%$. The average pressure of the whole plateau phase was 4564.2 ± 317.9 Pa. The plateau phase in PE35 on average started at a strain of $10.6 \pm 0.3\%$ and pressure of 4665.3 ± 422.5 Pa and lasted till a strain of $44.4 \pm 0.1\%$ and pressure of 5641.0 ± 532.6 Pa. The average plateau pressure was 5221.7 ± 217.2 Pa. The start and end pressure of the plateau phase

in PE40 was 4898.0 ± 173.2 Pa and 6082.0 ± 103.9 Pa respectively. The corresponding strain is $9.8 \pm 0.1\%$ and $44.6 \pm 0.1\%$. The average plateau pressure in PE40 was 5594.3 ± 274.9 Pa. The initial plateau pressure and strain in PU40 was 2873 ± 241.6 Pa and $9.7 \pm 0.1\%$. The plateau phase ended at 3614.0 ± 281.9 Pa and a strain of $39.8 \pm 0.2\%$. In PU40 the average plateau pressure was 3267.5 ± 207.7 Pa. In MF, the average pressure during the plateau phase was 1375.6 ± 178.7 Pa. The plateau phase started at an average strain of $7.7 \pm 0.3\%$ and pressure of 1105.3 ± 12.7 Pa and ended at an average strain and pressure of $49.6 \pm 0.1\%$ and 1829.3 ± 43.9 Pa. In figure 6, the average stress-strain curve of each foam type can be found.

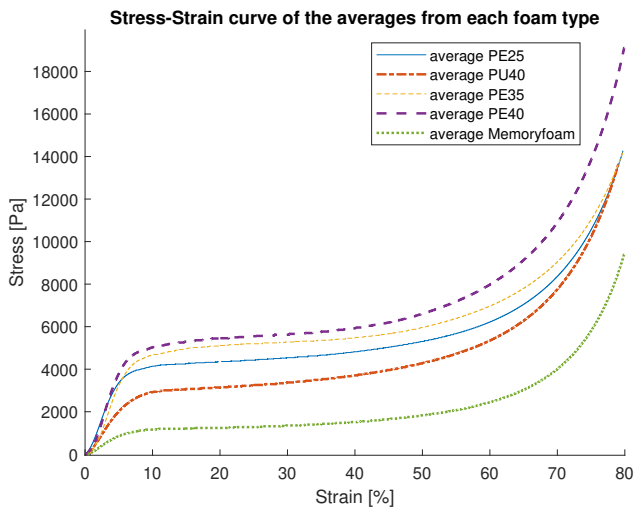


Fig. 6. The average stress-strain curve obtained from the compression test with a displacement rate of 0.1 mm/s of the different polymer foam samples with a dimension of 50x50x50 mm.

The average plateau stress for the different polymer foams can be found in table 1. One of the requirements of the filler material is that it provides sufficient support so that the reduction is maintained throughout the cast treatment while preventing CS. It was established that pressure in the SMC should be 2652.1 ± 93.2 Pa and that the pressure should remain under 3333.06 Pa to prevent CS. This pressure falls in between the average plateau pressure of PU40 and MF. Therefore, the other polymer foams PE25, PE35

Table 1. The average stress of the plateau phase and the strain period of the plateau phase obtained from the compression test for each type of polymer foam. The suitable polymer foams are highlighted in green

Foam Type	Average Plateau Stress		Plateau Phase
	[Pa] (mean±SD)	[mmHg] (mean±SD)	[begin-end %]
PE25	4564.2±317.9	34.2±2.4	7.7-49.6
PE35	5221.7±217.2	39.2±1.6	10.6-44.4
PE40	5594.3±274.9	42.0±2.1	9.8-44.6
PU40	3267.5±207.7	24.5±1.6	9.7-39.8
MF	1375.6±178.7	10.3±1.3	7.7-49.6

and PE40 are too stiff to be used in the SMC and can be disregarded. While the MF provides only 51.8% of the pressure needed during the plateau phase, the PU40 foam sample maintains a pressure that is 23.2% higher than the desired pressure level. Both the average plateau pressure in MF and PU40 remains under the pressure that could cause CS. The end plateau phase pressure of PU40, 3614.0 ± 281.9 , is higher than the safe threshold value for CS. However, to prove the concept of a smart memory cast, a cast that can maintain constant pressure regardless of the degree of swelling in the soft tissue during the treatment period, MF and PU40 can both be used.

In MF and PU40, the plateau phase begins at a strain of $7.7 \pm 0.3\%$ and $9.7 \pm 0.1\%$ respectively. Therefore, the MF and PU40 should be pre-compressed such that when the cast is applied, the foam is in the plateau phase.

B. Sensor Calibration

In figure 7, the stress-strain curves of PU40 and MF are plotted combined with the operating range of the 406 FSR sensor. The operating range of the 406 FSR sensor combined with PU40 is from 1166 Pa, which corresponds with a 12.5% strain, up to 7290 Pa and a strain of 80%. Com-

bined with MF, the operating range of the 406 FSR starts at 932.5 Pa and ends at 2246 Pa. This correlates with a 56% strain up to an 80% strain. In figure 8, the stress-strain curve is plotted from the compression test of PU40 and MF in combination with the SEN0295 sensors. The red box in these plots represents the operating range of the sensor for that specific foam type. The SEN0295 sensor combined with PU40 has an operating range from 296.7 Pa up to 6570 Pa and from 8.6 % to 80% strain. The operating range from SEN0295 paired with MF ranges from 1399 Pa till 2289 Pa and 59.7 % - 80% strain.

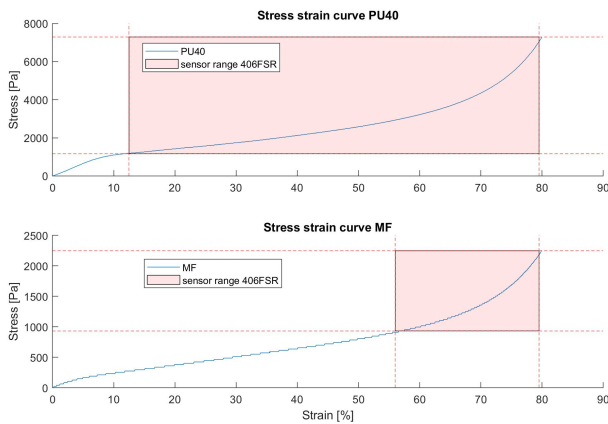


Fig. 7. The sensitivity range of the 406 FSR sensor combined with the stress-strain curve of a PU40 and MF sample with the same thickness of 20 mm as the filler material in the smart memory cast.

In figure 7, the difference in sensitivity range for the 406 FSR sensor in combination with MF or PU40 can be seen. The 406 FSR sensor combined with PU40 results in a sensitivity range that covers the plateau phase of the foam, from 9.7% - 39.8% strain. While with MF the sensitivity range of the sensor contains mostly the densification phase, from 49.7 % - 80% strain, since the plateau phase ended around a strain of 49.6 %. In this densification phase, the pressure increases exponentially. Since the filler material should maintain a constant pressure regardless of the degree of swelling, the plateau phase of the foam should be covered by the operating range of the sensor used. The same results were seen in the other 406 FSR sensors tested.

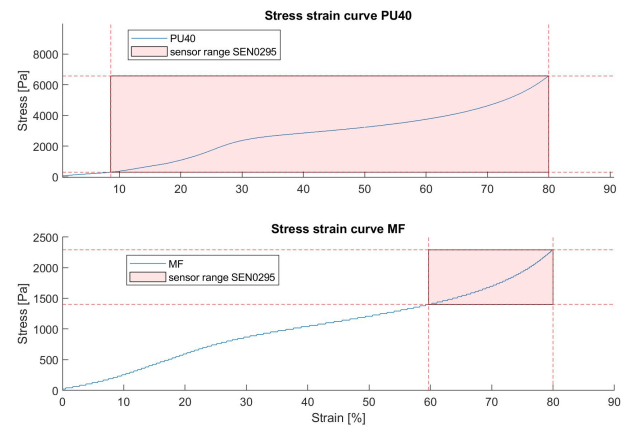


Fig. 8. The sensitivity range of the SEN0295 sensor combined with the stress-strain curve of a PU40 and MF sample with the same thickness of 20 mm as the filler material in the smart memory cast.

The results of the SEN0295 sensor combined with MF are similar to that of the 406 FSR sensor with MF, see figures 7 and 8. The operating range, 59.7% - 80 % strain, only covered a part of the densification phase of the MF, 49.6% - 80% strain. The operating range of SEN0295 paired with PU40, 8.6% - 80% strain, covered the plateau phase of PU40, 9.7% - 39.8% strain.

According to the datasheet of the SEN0295 sensor and the 406FSR sensor the operating range from these sensor should cover the plateau phase of the MF from the results in figure 6 and table 1 [39, 40]. However, non of the pressure sensors analysed were sensitive enough to measure pressure in combination with MF. It is hypothesised that may result from the visco-elastic properties of MF.

While the sensitivity varied from sensor to sensor, 4 of the 406FSR sensors and 7 of the SEN0295 sensors proved suitable for measuring the PU40 foam. Since 6 sensors were needed for the subsequent experiments with the SMC, it was opted to use six of individually calibrated SEN0295 sensors. All the sensors showed non-linear behavior. This non-linear behavior was different in each sensor. To address the sensitivity issues from both sensors in future research, there could be looked at thin film pressure sen-

sors that have a larger force sensitivity range than the sensors used in this research. More information about the calibration of the sensors and the sensitivity range of each sensor individually can be found in appendix D.

C. Smart Memory Cast

To prevent the silicone from rupturing during testing with the TC, all three parts of the TC were filled with a smaller amount of water as can be seen in figure 10.

In the wrist segment in the SMC, the red zone in figure 9, the pressure plateaued after 5 ml of water had been added. At this point, the pressure measured in the wrist top (WT) sensor and wrist bottom (WB) sensor is 1936.7 Pa and 2769.8 Pa respectively, see figures 10c and 10d. After 7 ml of water had been pushed into the wrist in the TC the pressure went above the operating range of the WB sensor which corresponds with 4728.0 Pa. At the end of the filling phase, the pressure measured in the WT sensor in the SMC was 2906.4 Pa and in the TC 5177.3 Pa. In the WB sensor in the SMC, the highest pressure was 3120.0 Pa. In the SMC the pressure measured by the WT and WB sensors remained under the pressure of 3333.06 Pa (25 mmHg) which could result in CS. The pressure decrease during the 5-minute interval was of comparable magnitude in the WT sensor in the SMC and TC, precisely 459.2 Pa and 448.3 Pa, respectively. In the WB sensor in the SMC, the pressure dropped with 85.3 Pa. Figure 11 shows that when all of the water was drained from the wrist section and the sensors were left operating for 5 minutes, the pressure recovered to 198.4 Pa and 232.2 Pa in the SMC and TC, respectively.

In the forearm segment, which corresponds to the green region in figure 9, the pressure in the SMC reached a plateau at 2102.6 Pa in the forearm top (FT) sensor and at 3244.4 Pa in the forearm bottom (FB) sensor (Figures 10e and 10f). The pressures measured at the end of the swelling were 2542.9 Pa in the FT sensor and 3476.3 Pa in the FB sensor in the SMC. This final

pressure in the FB sensors surpassed the safe threshold pressure for CS. Meanwhile, after injecting 3.6 ml of water into the forearm, the pressure in the TC sensor exceeded 5363.0 Pa, which is the maximum limit of the FT sensor's range. The pressure in the FB sensors kept increasing as the segment was filled with water in the TC and measured 5063.6 Pa at the end of the filling phase. In both the SMC and the TC, the pressure on the artificial arm decreased during the 5-minute rest. This decrease in the SMC was greatest in the FB sensor, with a drop of 433.4 Pa, and in the FT sensor, with a loss of 247.5 Pa. In the TC, there was only a decrease of 36.3 Pa.

In both the SMC and TC the pressure kept increasing as more water was pushed into the hand segment, the yellow area in figure 9, as can be seen in figures 10a and 10b. The hand bottom (HB) sensor recorded the maximum pressure in the SMC at 2373.2 Pa near the end. The highest pressure registered in the hand top (HT) sensor occurred when 46.45 ml of water was injected at 2029.3 Pa. In both these results, there was not a distinguishable plateau phase as in the wrist and forearm part. In the TC, the pressures detected by the HT and HB sensors were 3729.8 Pa and 4177.2 Pa, accordingly. During the 5-minute break the pressure in the SMC in the HT sensor dropped with 276 Pa and in the HB sensor with 43 Pa, while in the TC, the pressure dropped with 30.1 Pa in the HT sensor and increased with 104.7 Pa in the HB sensor.

In figure 12, in the WT and WB sensors, the average pressure in the SMC on the wrist was respectively 1442 and 2846 Pa. The pressures observed in the WT and WB sensors in the TC were greater, at 4355 and 4743 Pa, accordingly. The highest average pressure was detected in the TC was 5343 Pa in the FT sensor and in the FB the pressure was 4371 Pa. In the SMC the pressure was reduced to 2158 and 2004 Pa in the FT and FB sensor. The lowest pressure was seen in the TC in the HT sensor at 732.5 Pa, compared to 1401 Pa in the SMC HT sensor. The pressure in the HB sensor in the TC was 4011 Pa as opposed



Fig. 9. The different parts of the forearm that are inflated to mimic soft tissue swelling from left to right: the hand (yellow), the wrist (red) the forearm (green).

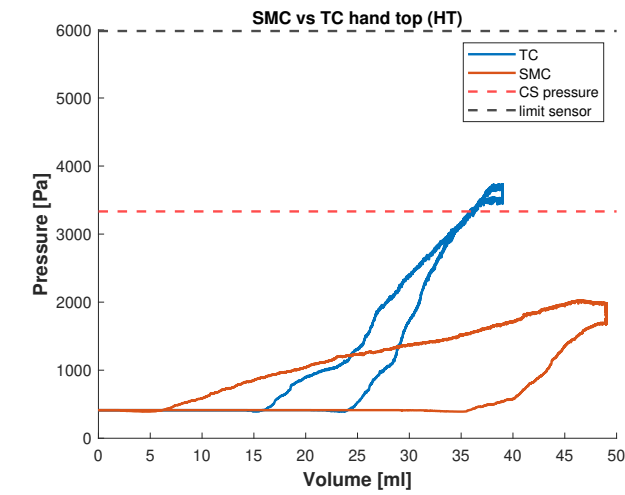
to 2474 Pa in the SMC.

From the results in figure 10, it could be seen that in the SMC the pressure increased more gradually compared to in the TC. The stiff nature of cast material, Delta-cast[®], caused the pressure inside the TC to increase more rapidly as each part was inflated. Furthermore, due to the material properties of the PU40 filler material in the SMC, in the wrist and forearm segment in the SMC the pressure approached the low-stiffness plateau, as previously indicated in the foam stiffness experiments in figure 6. This plateau phase was not seen in the hand segment pressure readings. This could be due to the shape of the hand. The sensor placed on the bottom part of the hand covered the palm. Considering the concave shape of the palm, the PU40 foam may not have been uniformly compressed. Therefore, due to the anisotropic nature of polymer foams, the pressure measurements may have been affected [37, 41–43].

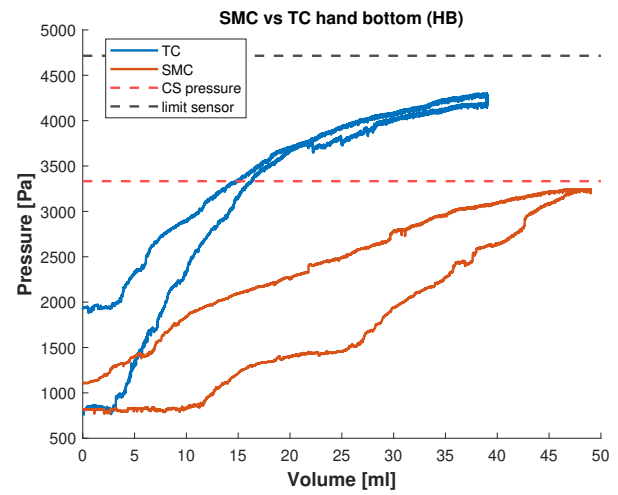
In the pressure readings of the WB sensor in figures 10d and 12 and of the FT sensor in figure 10e in the TC, the pressure went beyond the operating range of the sensors and therefore the sensors were no longer able to give a reliable reading.

In all the segments, except in the FB sensor, that were analysed in figure 10 and 12, the pressure measured in the SMC was reduced to below the safe threshold value that could cause CS. The average pressure in the SMC was reduced by 47.8%, figure 12, and remained under the pressure that could cause CS. The pressure in the wrist in the SMC was reduced by 40% in the bottom sensor and 66.9% at the top compared to the TC. In the forearm, the pressure decreased by more than 50% in both parts. In the HT sensor, the pressure in the SMC increased by 91% compared to the TC. It increased from 732.48 Pa in TC to 1400.7 Pa in the SMC. So, the final pressure measured in the SMC is still below the CS value of 3333.06 Pa. Only in the WB sensor in the TC, the pressure measured of 4743.1 Pa, exceeded the operating range of the sensor. The amount of water injected in each segment in the TC cast was 10 ml less than in the SMC. In addition, the sensors were only calibrated with the PU40 layer and not with the cotton layer and stockinette used in the TC. Therefore, the pressure in the TC may be higher than measured with the sensors.

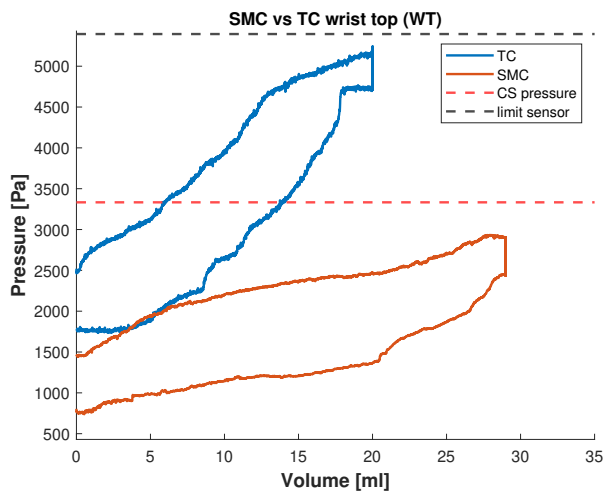
In figures 10 and 11, it can be seen that relaxation occurred in the filler material, as there was a



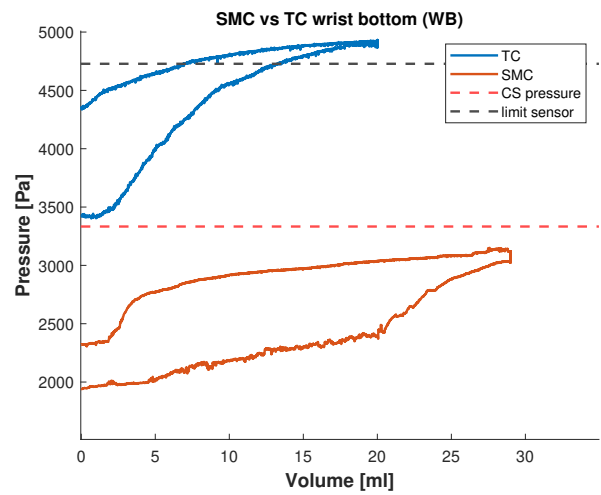
(a)



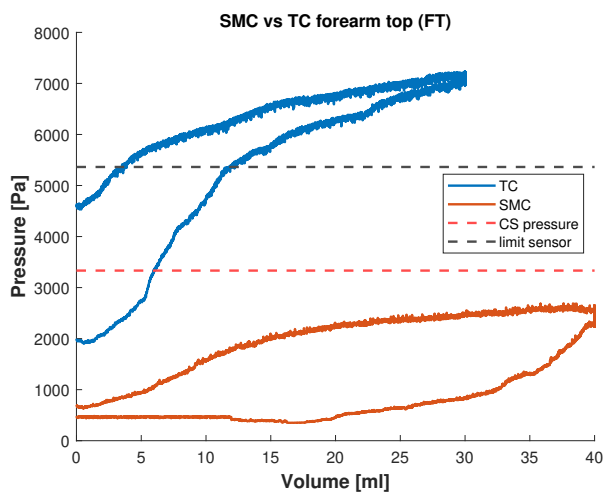
(b)



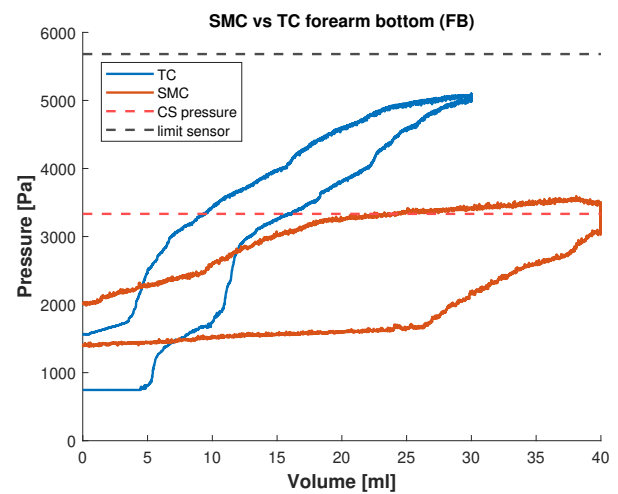
(c)



(d)



(e)



(f)

Fig. 10. In 10a -10f, the pressure versus volume results from the hand, wrist and forearm segment in the SMC and TC are plotted. The red striped line is the safe threshold value of 25 mmHg to prevent CS and the black striped line is the upper limit of the operating range of the sensor.

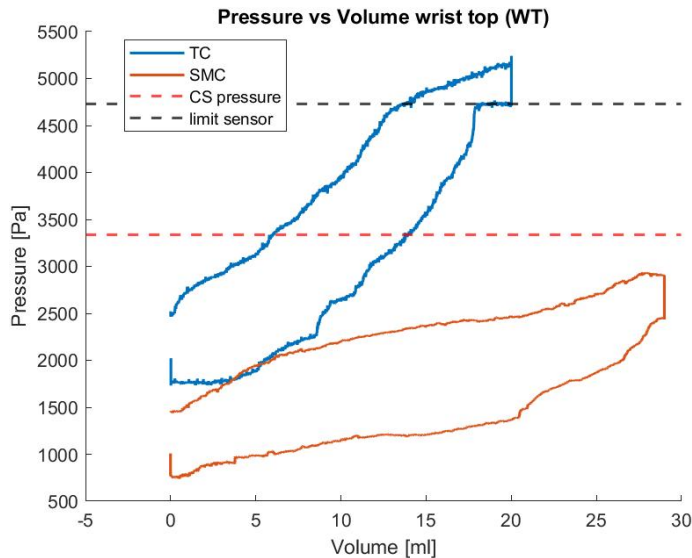


Fig. 11. The pressure measured in the top sensor on the wrist while water is injected and withdrawn from the part. After it was filled, there was a 5-minute pause before the water was withdrawn. Lastly, the sensors kept running for 5 more minutes after the part was emptied.

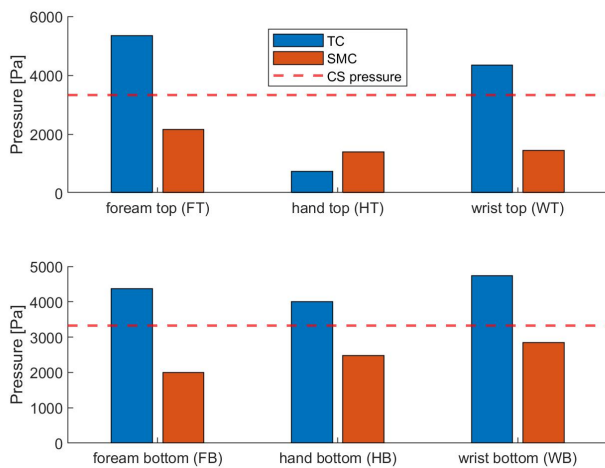


Fig. 12. The average pressure in the SMC and TC after each segment was filled with water five times repeatedly. In the SMC the hand, forearm and the wrist were filled with 49 ml, 40 ml and 29 ml respectively. While in the TC, 39 ml, 30 ml and 19 ml of water was injected.

pressure drop when the segment has been filled while kept at rest for 5 minutes. This relaxation behaviour was larger in the SMC than in the TC.

Additionally, the hysteresis loss was also larger in the SMC than in the TC. In both the casts, after the segment was deflated, stress recovery occurred. In the TC, this could result from the segment settling back to its original shape after the water was withdrawn and thus pushing back against the rigid cast thereby increasing the pressure. In the SMC due to the visco-elastic properties of PU40, the foam recovered back to its original shape and thus increased the pressure again. In the SMC and TC, this stress recovery was of similar magnitude.

These results indicate that the SMC was capable of decreasing stress concentration while providing the support stiffness compared to the TC. Furthermore, it also reduced the overall pressure on the artificial arm such that the risk for CS is mitigated. However, none of the pressures measured in the SMC were within the pressure range of 2652.1 ± 93.2 Pa needed to keep a DRF reduced. The PU40 foam did not provide the required stiffness to maintain the reduction.

More pressure readings from experiments with the SMC and TC can be found in appendix E.

D. Recommendations

The soft polymer foam PU40 utilized in the SMC experiments might reduce stress concentration, yet it was too stiff. As a result of this, the pressure in the cast was higher than the pressure needed to maintain a reduction of the DRF. This could be resolved by using a material whose plateau phase is within this range, a softer material, or by making alterations to the surface of the foam to change the mechanical properties. An alternative solution could be combining different foam types to obtain the desired properties. Another type of material that can be considered is soft mechanical meta-materials. By altering the geometrical structure of the material, the material properties can be tuned to the desired one [43–47].

The pressure recovery in the SMC after the swelling had decreased was of the same order as in the TC. By introducing a filler material that has higher visco-elastic properties such as mem-

ory foam (MF), this recovery could be increased [48–51].

When the synthetic cast for the SMC was applied to the artificial arm, the PU40 layer had already been cut in a rectangular shape with the desired dimensions and was wrapped around the arm. The cast technician only had to wrap the Delta-cast® conformable material around the arm. It would have been a strenuous task for the cast technician to wrap the foam layer as well as the cast material by himself. Therefore, it should be investigated whether it is possible to make the foam layer such that it has the shape of a sleeve that can be pulled over the forearm instead wrapped around it.

Another important aspect is patient comfort. The cotton layer in a TC retains water and dries slowly. This can cause skin irritation and itchiness when it gets wetted by sweat that is released through the skin to regulate body temperature or by accident. Therefore, the gas permeability of the filler material should be further investigated since it is in close contact with the skin and it may absorb perspiration. The moisture should be able to evaporate quickly such that it does not cause any skin irritation or damage [48, 52–54].

During the physical examination of a patient with a distal radius fracture, it was seen that this type of fracture is often accompanied by wrist oedema [55–57]. Considering the swelling influences the thickness of the filler material used, an understanding of soft tissue swelling immediately after a DRF, as well as for the duration of the treatment would be needed. However, limited research can be found on this [30, 58]. Additionally, there is also limited knowledge about how much the pressure in the cast should be to keep a DRF reduced. Most research evaluates the skin surface pressure and the intracompartmental pressure such that CS and skin damage can be prevented [34, 59, 60]. When the intracast pressure needed to maintain a reduction of the DRF is known, a filler material can be chosen that fulfils the new requirements. The SMC will then have to be evaluated again with the artificial arm until the correct filler material is found.

Such that in the end the SMC can be examined in clinical trials.

Further, the cast mould quality is not the only risk factor that affects the re-displacement rate of reduced DRFs. The initial fracture type and displacement are also associated with treatment failure. The quality of the reduction is a significant indicator with regard to the risk of re-displacement of the fracture as well. Re-displacement is a complication not caused by a single factor but by multiple factors and should be assessed as one. Therefore, it is also important that the success of the initial reduction performed by the orthopaedic surgeon is assessed as well [17, 61–63].

4. CONCLUSION

In this research the effectiveness of a smart memory cast to relieve stress concentration while providing the required support stiffness compared to a traditional cast is studied. While the segments of the artificial arm were swelling, the pressure in the smart memory cast plateaued due to the material properties of the PU40 filler material used. The pressure measured in the smart memory cast stayed below the threshold pressure that could cause compartment syndrome. In the traditional cast, the pressure kept increasing as the segments were inflating and the measurements indicated that compartment syndrome could occur. However, in the smart memory cast the pressure only plateaued after a certain degree of tissue swelling. To tackle this issue, a more flexible filler material that has the required support stiffness, a wide plateau stiffness, that can be placed easily with error tolerance, that supports shocks, and relaxes upon swelling has to be created. There has been little research done about the needed pressure range to keep a distal radius fracture reduced and soft tissue swelling after this type of fracture. Therefore, complementary research needs to be done about these topics such that more information about the desired material properties for the filler material is available and different materials can be examined as well.

Acknowledgement

I want to thank my supervisors Dr Andres Hunt (TU Delft), Dr Shahram Janbaz (UvA) and Dr Joost Colaris (Erasmus MC) for their help and guidance with the project. Furthermore, I want to thank the casting technician, mr. R. van de Lugt, for his time and for providing me with the materials needed for the smart memory cast as well as the traditional cast. I wish to thank the people, mr. J. van Driel and mr. J. Brenkman, of the meetshop for their help with the set-up of the experiments.

REFERENCES

- N. J. MacIntyre and N. Dewan, "Epidemiology of distal radius fractures and factors predicting risk and prognosis," *J. Hand Ther.* **29**, 136–145 (2016). Special Issue: Wrist.
- S. Polinder, G. I. Iordens, M. J. Panneman, D. Eygendaal, P. Patka, D. Den Hartog, and E. M. Van Lieshout, "Trends in incidence and costs of injuries to the shoulder, arm and wrist in the netherlands between 1986 and 2008," *BMC Public Heal.* **13** (2013).
- K. W. Nellans, E. Kowalski, and K. C. Chung, "The epidemiology of distal radius fractures," *Hand Clin.* **28**, 113–125 (2012).
- Y. Ochen, J. Peek, D. van der Velde, F. J. Beeres, M. van Heijl, R. H. Groenwold, R. M. Houwert, and M. Heng, "Operative vs nonoperative treatment of distal radius fractures in adults," *JAMA Netw. Open* **3** (2020).
- K. O. Koo, D. M. Tan, and A. K. Chong, "Distal radius fractures: An epidemiological review," *Orthop. Surg.* **5**, 209–213 (2013).
- J. Ye, Q. Li, and J. Nie, "Prevalence, characteristics, and associated risk factors of wrist fractures in americans above 50: The cross-sectional nhanes study," *Front. Endocrinol.* **13** (2022).
- C. de Putter, E. van Beeck, C. Looman, H. Toet, S. Hovius, and R. Selles, "Trends in wrist fractures in children and adolescents, 1997–2009," *The J. Hand Surg.* **36** (2011).
- D. Jerrhag, M. Englund, M. K. Karlsson, and B. E. Rosengren, "Epidemiology and time trends of distal forearm fractures in adults - a study of 11.2 million person-years in sweden," *BMC Musculoskelet. Disord.* **18** (2017).
- J. Rundgren, A. Bojan, C. Mellstrand Navarro, and A. Enocson, "Epidemiology, classification, treatment and mortality of distal radius fractures in adults: An observational study of 23,394 fractures from the national swedish fracture register," *BMC Musculoskelet. Disord.* **21** (2020).
- J. L. Francis, J. M. Battle, J. Hardman, and R. E. Anakwe, "Patterns of injury and treatment for distal radius fractures at a major trauma centre," *Bone amp; Jt. Open* **3**, 623–627 (2022).
- W. P. Mosenthal, H. H. Boyajian, S. A. Ham, and M. A. Conti Mica, "Treatment trends, complications, and effects of comorbidities on distal radius fractures," *HAND* **14**, 534–539 (2018).
- A. Azad, H. P. Kang, R. K. Alluri, V. Vakhshori, H. F. Kay, and A. Ghiassi, "Epidemiological and treatment trends of distal radius fractures across multiple age groups," *J. Wrist Surg.* **08**, 305–311 (2019).
- L. Kong, J. Lu, Y. Zhou, D. Tian, and B. Zhang, "Incidence and risk factors for redisplacement after closed reduction and instant rigid cast immobilization for paediatric distal radius fractures: A case control study," *J. Orthop. Surg. Res.* **15** (2020).
- V. Pavone, A. Vescio, L. Lucenti, E. Chisari, F. Canavese, and G. Testa, "Analysis of loss of reduction as risk factor for additional secondary displacement in children with displaced distal radius fractures treated conservatively," *Orthop. amp; Traumatol. Surg. amp; Res.* **106**, 193–198 (2020).
- S. M. LaValva, B. H. Rogers, A. Arkader, and A. S. Shah, "Risk factors for failed closed reduction of pediatric distal radius fractures," *J. Hand Surg. Glob. Online* **2**, 196–202 (2020).
- A. Turgut, S. Erkuş, A. Koca, L. Payzıner, A. O. Çiçek, and Önder Kalenderer, "Analysis of the factors causing tight cast syndrome after closed reduction and casting of pediatric distal radius fractures," *Acta Orthop. et Traumatol. Turcica* **52**, 329–333 (2018).
- R. Arora, P. Mishra, A. N. Aggarwal, R. Anshuman, and R. Sreenivasan, "Factors responsible for redisplacement of pediatric forearm fractures treated by closed reduction and cast," *Indian J. Orthop.* **52**, 536–547 (2018).
- K. Bin, L. Rony, N. Henric, and D. Moukoko, "Pediatric fracture reduction in the emergency department," *Orthop. amp; Traumatol. Surg. amp; Res.* **108**, 103155 (2022).
- K. B. Alemdaroğlu, S. İltar, O. Çimen, M. Uysal, E. Alagöz, and D. Atlıhan, "Risk factors in redisplacement of distal radial fractures in children," *The J. Bone amp; Jt. Surg.* **90**, 1224–1230 (2008).
- T. McKinley, "Principles of fracture healing," *Surg. (Oxford)* **21**, 209–212 (2003).
- G. Cheing, J. Wan, and S. Kai Lo, "Ice and pulsed electromagnetic field to reduce pain and swelling after distal radius fractures," *J. Rehabil. Medicine* **37**, 372–377 (2005).
- F. Tull and J. Borrelli, "Soft-tissue injury associated with closed fractures: Evaluation and management," *J. Am. Acad. Orthop. Surg.* **11**, 431–438 (2003).
- C. J. Zaino, M. R. Patel, M. S. Arief, and R. Pivec, "The effectiveness of bivalving, cast spreading, and webril cutting to reduce cast pressure in a fiberglass short arm cast," *J. Bone Jt. Surg.* **97**, 374–380 (2015).
- M. Halanski and K. J. Noonan, "Cast and splint immobilization: Complications," *J. Am. Acad. Orthop. Surg.* **16**, 30–40 (2008).
- N. Kvatinsky, R. Carmiel, R. Leiba, and I. Shavit, "emergency department revisits due to cast-related pain in children with forearm fractures," *J. Pain Res.* **Volume 13**, 11–16 (2020).
- D. J. Slutsky and M. Herman, "Rehabilitation of distal radius fractures: A biomechanical guide," *Hand Clin.* **21**, 455–468 (2005).
- R. Wytch, P. Ashcroft, C. Kalisse, G. Neil, N. Ross, and D. Ward, "Interface pressures in below elbow casts," *Clin. Biomech.* **6**, 25–30 (1991).
- J. Patrick and B. Levack, "A study of pressures beneath forearm plasters," *Injury* **13**, 37–41 (1981).
- J. Moir, R. Wytch, G. Ashcroft, G. Neil, N. Ross, and D. Wardlaw, "Intracast pressure measurements in colles' fractures," *Injury* **22**, 446–450 (1991).
- A. Younger, P. Curran, and M. McQueen, "Backslabs and plaster casts: which will best accommodate increasing intracompartmental pressures?" *Injury* **21**, 179–181 (1990).
- S. Nguyen, M. McDowell, and J. Schlechter, "Casting: Pearls and pitfalls learned while caring for children's fractures," *World J. Orthop.* **7**, 539 (2016).
- D. I. Davis and M. Baratz, "Soft tissue complications of distal radius fractures," *Hand Clin.* **26**, 229–235 (2010).
- S. J. Tharakan, U. Subotic, M. Kalisch, G. Staubli, and D. M. Weber, "Compartment pressures in children with normal and fractured forearms: A preliminary report," *J. Pediatr. Orthop.* **36**, 410–415 (2016).
- M. M. Uslu and A. Apan, "Can skin surface pressure under a cast reveal intracompartmental pressure?" *Arch. Orthop. Trauma Surg.* **120**, 319–322 (2000).
- H.-K. Kao, Y.-C. Wu, C.-H. Lu, Z. Hua, M.-C. Chen, and C.-C. Tuan, "Application of simulated arms with real-time pressure monitor in casting and splinting by physiological sensors," *Sensors* **21**, 5681 (2021).
- P. Viot, "Hydrostatic compression on polypropylene foam," *Int. J. Impact Eng.* **36**, 975–989 (2009).
- L. Y. Gibson and F. R. Ashby, "The mechanics of three-dimensional cellular materials," *Proc. Royal Soc. Lond. A. Math. Phys. Sci.* **382**, 43–59 (1982).
- D. Eaves, *Handbook of polymer foams* (Rapra Technology, 2004).

39. "Description - sparkfun electronics," .
40. "Rp-c18.3-lt thin film pressure sensor - digi-key," .
41. P. Li, Y. Guo, M. Zhou, and V. Shim, "Response of anisotropic polyurethane foam to compression at different loading angles and strain rates," *Int. J. Impact Eng.* **127**, 154–168 (2019).
42. N. Mills, "Polymer foams for personal protection: Cushions, shoes and helmets," *Compos. Sci. Technol.* **63**, 2389–2400 (2003).
43. B. E. Obi, *Polymeric foams structure-property-performance: A design guide* (William Andrew, 2018).
44. S. Maraghechi, J. Hoefnagels, R. Peerlings, O. Rokoš, and M. Geers, "Experimental full-field analysis of size effects in miniaturized cellular elastomeric metamaterials," *Mater. amp; Des.* **193**, 108684 (2020).
45. M. Jamshidian, N. Boddeti, D. Rosen, and O. Weeger, "Multiscale modelling of soft lattice metamaterials: Micromechanical nonlinear buckling analysis, experimental verification, and macroscale constitutive behaviour," *Int. J. Mech. Sci.* **188**, 105956 (2020).
46. M. Bodaghi, A. Damanpack, G. Hu, and W. Liao, "Large deformations of soft metamaterials fabricated by 3d printing," *Mater. amp; Des.* **131**, 81–91 (2017).
47. D. W. Holmes, D. Singh, R. Lamont, R. Daley, D. P. Forrestal, P. Slattery, E. Pickering, N. C. Paxton, S. K. Powell, M. A. Woodruff, and et al., "Mechanical behaviour of flexible 3d printed gyroid structures as a tuneable replacement for soft padding foam," *Addit. Manuf.* **50**, 102555 (2022).
48. D. Grzęda, G. Węgrzyk, M. Leszczyńska, L. Szczepkowski, M. Gloc, and J. Ryszkowska, "Viscoelastic polyurethane foams for use as auxiliary materials in orthopedics," *Materials.* **15**, 133 (2021).
49. S. W. White, S. K. Kim, A. K. Bajaj, P. Davies, D. K. Showers, and P. E. Liedtke, "Experimental techniques and identification of nonlinear and viscoelastic properties of flexible polyurethane foam," *Nonlinear Dyn.* **22**, 281–313 (2000).
50. S. Hager and T. Craig, "Fatigue testing of high performance flexible polyurethane foam," *J. Cell. Plast.* **28**, 284–303 (1992).
51. K. Vorphohl, J. Mertes, R. Zschiesche, H.-D. Lutter, and R. Drumm, "Time dependence of hardness of cold cure molded flexible foams and its importance for system development," *J. Cell. Plast.* **30**, 361–374 (1994).
52. M. Zhu, E. Lokino, C. Chan, A. Gan, L. Ong, and K. Lim, "Cast immobilisation for the treatment of paediatric distal radius fracture: Fibreglass versus polyolefin," *Singapore Med. J.* **60**, 183–187 (2019).
53. C. R. Wolff and P. James, "The prevention of skin excoriation under childrens hip spica casts using the goretex pantaloon," *J. Pediatr. Orthop.* **15**, 386–388 (1995).
54. P. Srb and R. Martonka, "Mechanical properties of polyurethane foam in different climate conditions," in *Modern Methods of Construction Design*, L. Ševčík, P. Lepšík, M. Petrú, I. Mašín, and R. Martonka, eds. (Springer International Publishing, Cham, 2014), pp. 393–398.
55. A. P. Webster, "How do clinical features help identify paediatric patients with fractures following blunt wrist trauma?" *Emerg. Medicine J.* **23**, 354–357 (2006).
56. Y. Eyler, M. Sever, A. Turgut, N. Yalcin, N. Zafer, A. Suner, E. Aksay, and M. Yesilaras, "The evaluation of the sensitivity and specificity of wrist examination findings for predicting fractures," *The Am. J. Emerg. Medicine* **36**, 425–429 (2018).
57. S. H. Kozin and M. B. Wood, "Early soft-tissue complications after fractures of the distal part of the radius," *The J. Bone amp; Jt. Surg.* **75**, 144–153 (1993).
58. N. N. Byl, W. Kohlhase, and G. Engel, "Functional limitation immediately after cast immobilization and closed reduction of distal radius fractures: Preliminary report," *J. Hand Ther.* **12**, 201–211 (1999).
59. M. Mahirogullari, S. Surucu, M. H. Cerci, M. Aydin, A. Kayikli, and O. Gunduz, "Noninvasive technique to monitor the pressure under a cast: A mobile application-friendly bluetooth pressure sensor," *Int. J. Clin. Pract.* **2022**, 1–6 (2022).
60. J. R. DAVIDS, S. L. FRICK, E. SKEWES, and D. W. BLACKHURST, "Skin surface pressure beneath an above-the-knee cast," *The J. Bone amp; Jt. Surg.* **79**, 565–9 (1997).
61. A. G. McQuinn and R. L. Jaarsma, "Risk factors for redisplacement of pediatric distal forearm and distal radius fractures," *J. Pediatr. Orthop.* **32**, 687–692 (2012).
62. D. M. Constantino, L. Machado, M. Carvalho, J. Cabral, P. Sá Cardoso, I. Balacó, T. P. Ling, and C. Alves, "Redisplacement of paediatric distal radius fractures: What is the problem?" *J. Child. Orthop.* **15**, 532–539 (2021).
63. J. Pretell Mazzini and J. Rodriguez Martin, "Paediatric forearm and distal radius fractures: Risk factors and re-displacement—role of casting indices," *Int. Orthop.* **34**, 407–412 (2009).

A. APPENDIX: RESULTS COMPRESSION TEST

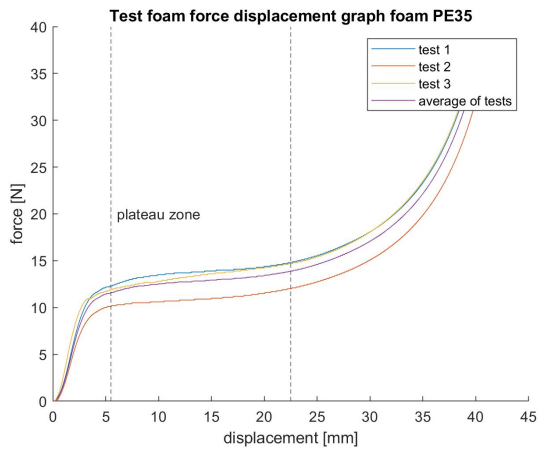
In this appendix, all the force-displacement curves obtained from the compression test are depicted in figure 13. As earlier mentioned, the strain rate during testing was 0.1 mm/s and the samples were compressed up until a strain of 80%. The data from the compression test is converted into the stress-strain curves seen in figure 14. For each polymer foam type, the individual data from the test are combined such that an averaged stress-strain curve could be obtained for each foam type. All the average stress-strain curves are then combined in figure 14f. For each foam type, three samples were tested, except for PE25 only two samples were tested. In all stress-strain curves, the three distinct phases that are known for polymer foams can be seen. First, there is a linear elastic phase in which the stress increases linearly as the strain increases. Next, a plateau phase occurs in which the stress almost does not increase as the foam sample is compressed which is followed by a densification phase in which the stress increases rapidly as the compression is further increased.

For the smart memory cast, the plateau phase is most important since that is the operating range of the new cast. The stress experienced during this plateau phase should be similar to the pressure needed to maintain a distal radius fracture reduced. In table 2, the average stress during the plateau phase for each foam type is calculated.

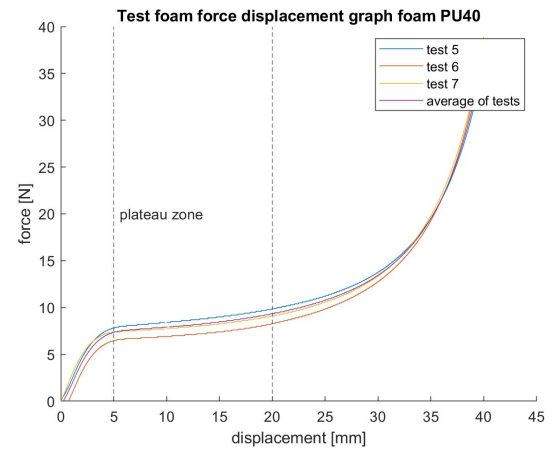
Table 2. The average stress was measured during the plateau phase for the different foam types PE25, PE35, PE40, PU40 and MF.

Foam Type	Mean [Pa]	SD [Pa]	Mean [mmHg]	SD [mmHg]
PE25	4564.2	317.9	34.2	2.4
PE35	5221.7	217.2	39.2	1.6
PE40	5594.3	274.9	42.0	2.1
PU40	3267.5	207.7	24.5	1.6
MF	1375.6	178.7	10.3	1.3

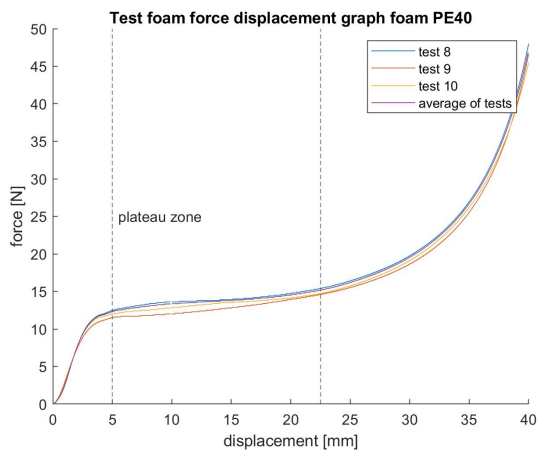
Besides to stress level of the plateau, the length of the plateau is also an important characteristic of the smart memory cast. The plateau phase should be long enough such that at the beginning of the treatment with the smart memory cast when the tissue swelling continues in the first few days the polymer foam is still compressed in this phase. Further, once the tissue swelling is reduced the filler material should decompress while still providing constant pressure to keep the distal radius fracture reduced. For the memory foam and PE25 foam, the plateau phase starts when the material is compressed at 7.7% of its original height. In the other materials PE35, PE40 and PU40 begin at respectively 10.6%, 9.8% and 9.7% strain. The plateau phase transitions into the densification phase at 49.6%, 49.6%, 44.4%, 44.6% and 39.8% strain for memory foam, PE25, PE35, PE40 and PU40 respectively. Therefore, memory foam has the longest plateau phase of all the polymer foam types tested, as can be seen in figure 14.



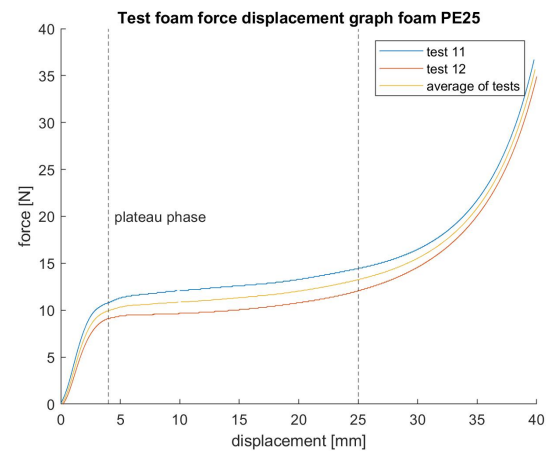
(a)



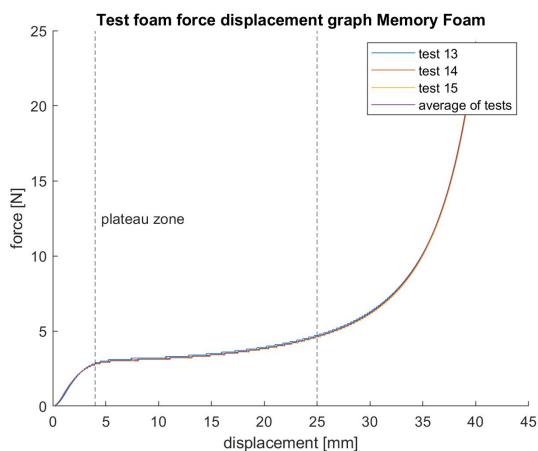
(b)



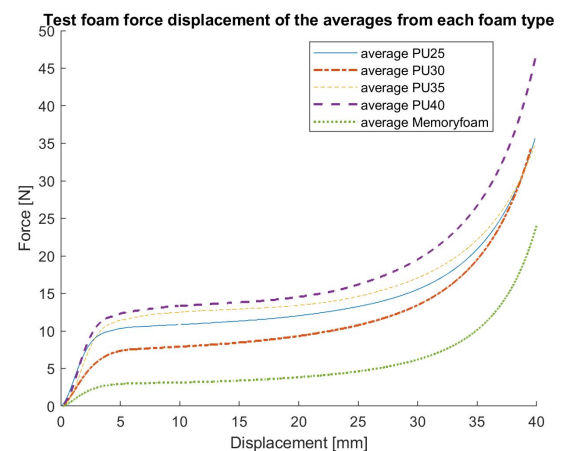
(c)



(d)



(e)



(f)

Fig. 13. Force-displacement curves obtained from compression tests performed on different polymer foam samples with dimensions 50x50x50mm and a displacement rate of 0.1 mm/sec and compression up to 80% of their original shape: 13a) PE35, 13b) PU40, 13c) PE40, 13d) PE25, 13e) MF. In 13f) the average from each foam type is combined.

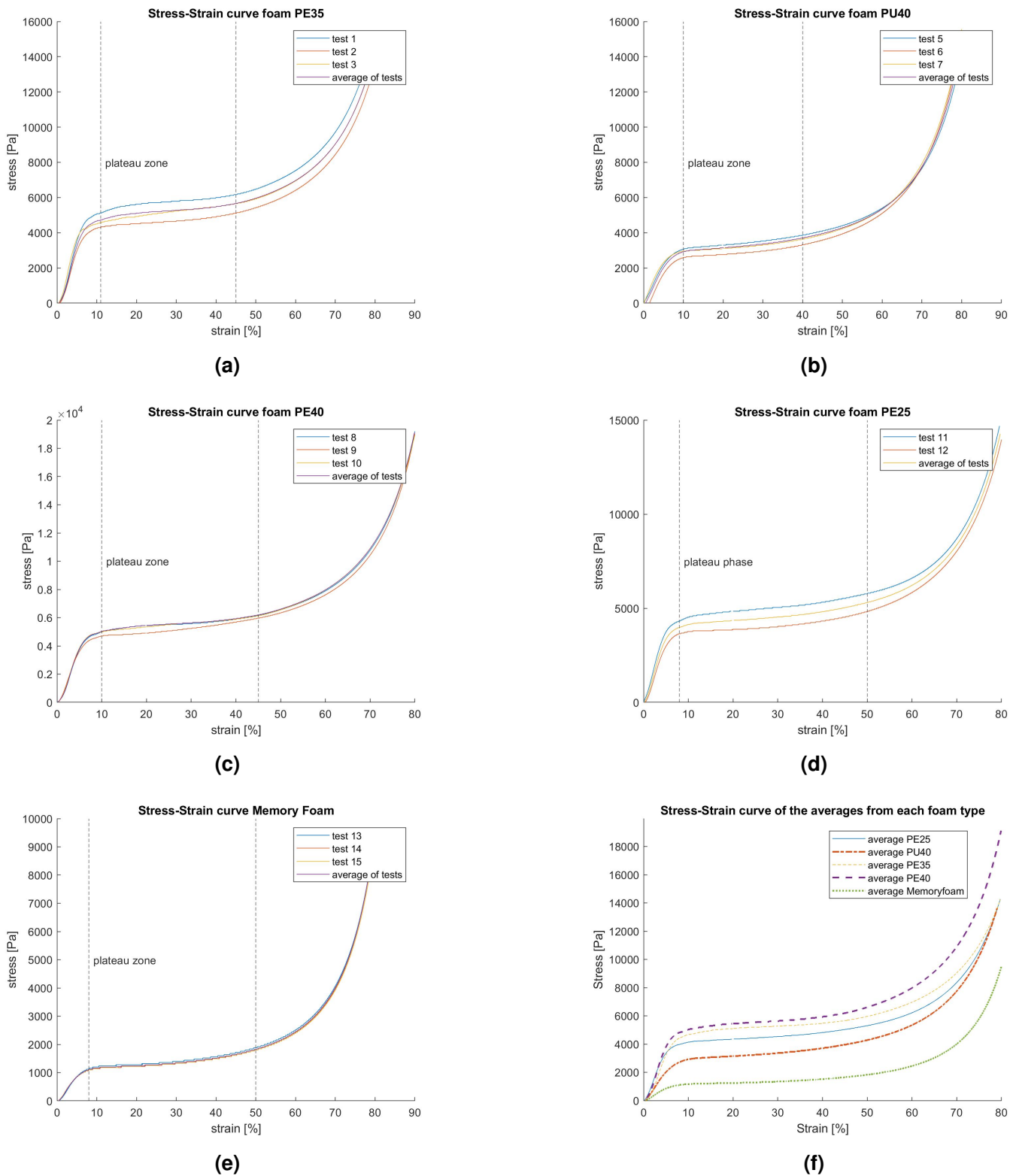
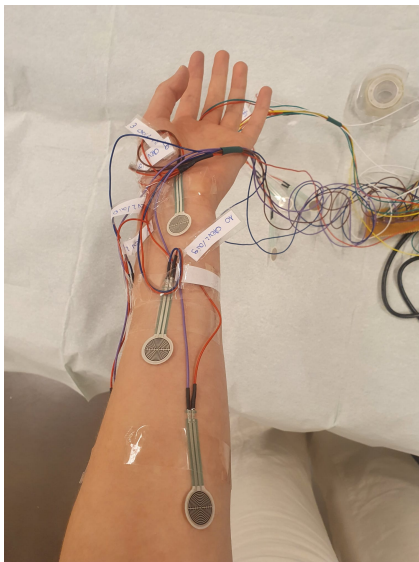


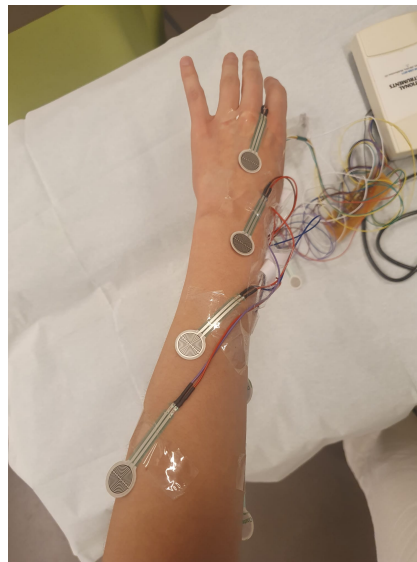
Fig. 14. The force-displacement curves from figure 13 transformed in to stress-strain curves from the different polymer foam samples: 14a) PE35, 14b) PU40, 14c) PE40, 14d) PE25, 14e) MF. In 14f) the average from each foam type is combined.

B. APPENDIX: RESULTS PRESSURE MEASUREMENTS UNDER A TRADITIONAL CAST

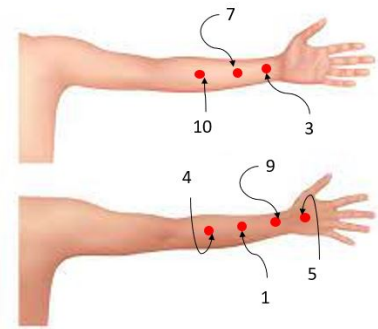
To choose a filler material from the tested polymer foam samples, the pressure that is needed to keep a fracture reduced should be known. Therefore, an experiment was done where the pressure on the skin was measured during the application and curing process of a traditional cast. The pressure was assessed by placing seven pressure sensors on the forearm. The position of the sensors can be seen in figure 15.



(a) Anterior side forearm



(b) Posterior side forearm

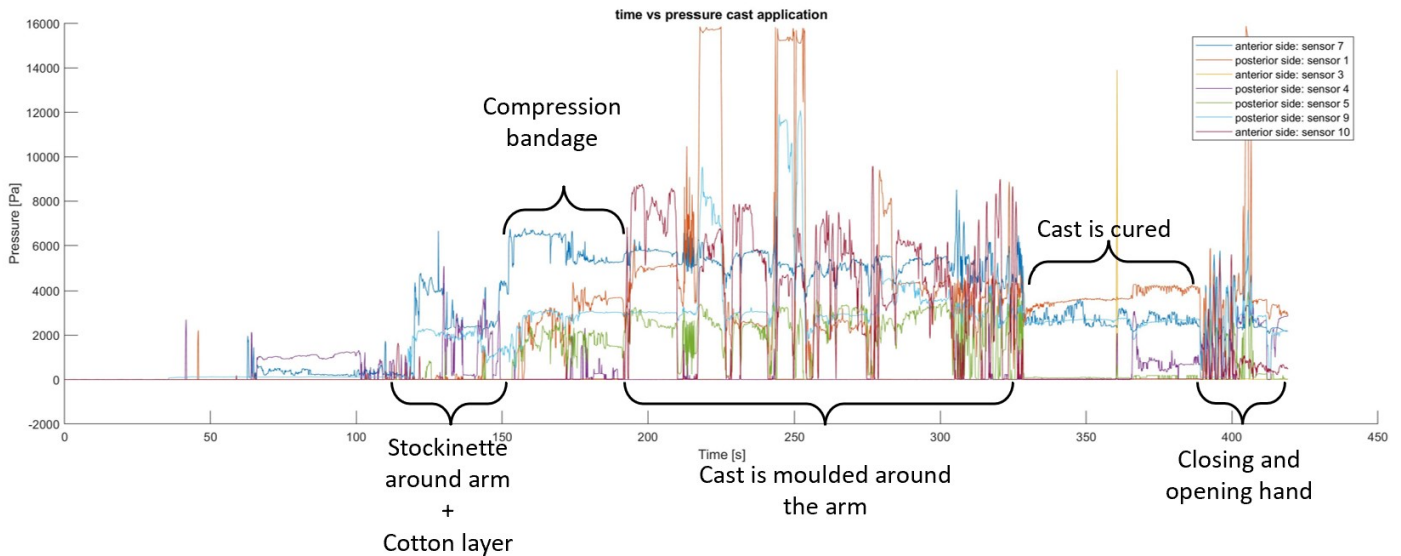


(c) Placement of the sensors on the anterior and posterior sides of the forearm

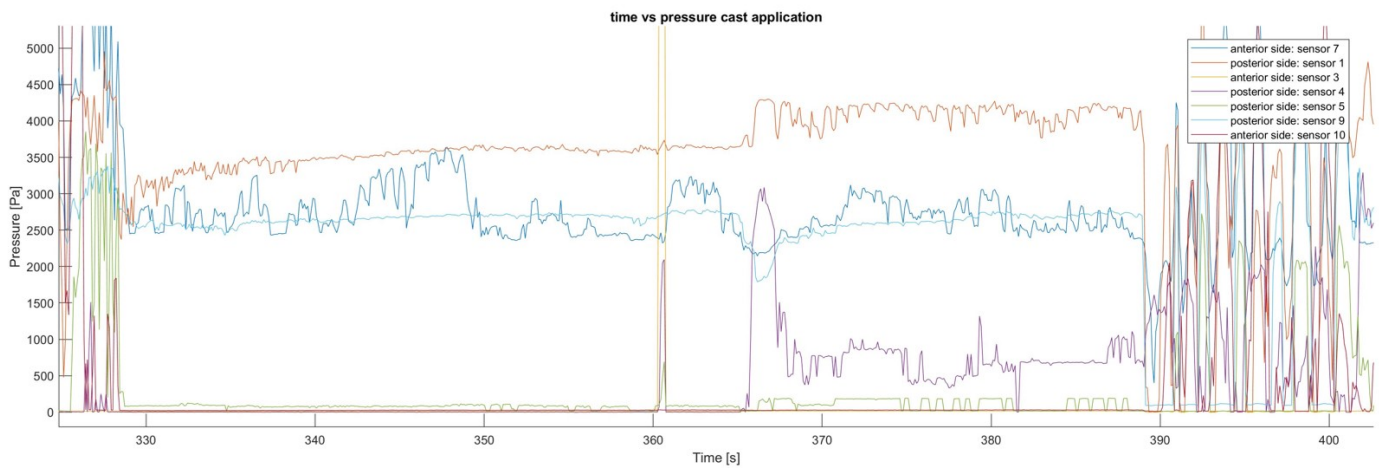
Fig. 15. Placement of the seven pressure sensors: three are positioned on the anterior side of the forearm and the other four are placed on the posterior side.

At Erasmus MC, the orthopaedic casting technician applied a circumferential below-elbow cast according to the guidelines in the Netherlands. First, a stockinette and cotton layer was placed over the arm, followed by a compression bandage. The Delta-cast[®] Conformable is dipped into room temperature water and wrapped around the arm. During the curing process of the cast, the orthopaedic casting technician moulds the cast around the arm by applying pressure to it such that it fits the shape of the arm. After five and a half minutes, the cast was completely cured. The pressure on the skin during the application process and once the cast was cured can be seen in figure 16.

The highest pressures once the cast was completely cured, were measured in sensors 1, 7 and 9. The value of the average pressure in the sensors can be seen in table 3. In the other sensors, the pressure measured is low compared to the pressure measured in sensors 1, 7 and 9 as can be seen in figure 16b. Therefore, they can be neglected.



(a)



(b)

Fig. 16. 16a) Pressure on the skin during the application of a below-elbow cast. 16b) The pressure on the skin once the cast was cured.

Table 3. The pressure was measured between the skin and cast in sensors 1, 7 and 9 once the cast was completely cured.

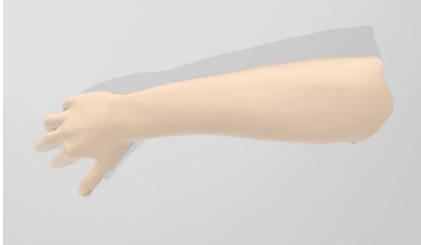
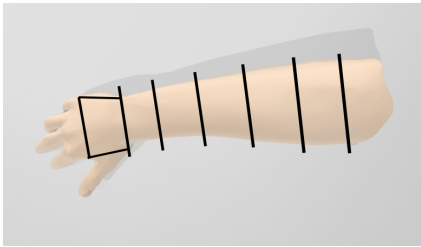
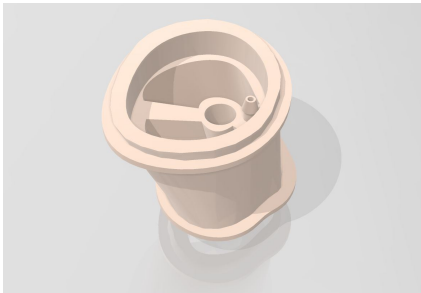
Sensor	Mean [Pa]	SD [Pa]	Mean [mmHg]	SD [mmHg]
1	3531.9	144.8	26.49	1.09
7	2751.4	338.2	20.64	2.54
9	2652.1	93.2	19.89	0.70

The fracture location of a distal radius fracture, more commonly known as a broken wrist, corresponds with the location of sensor 9. Therefore, the smart memory cast should produce a pressure that

approximates the pressure measured at that location, which is around 2652.1 Pa or 19.89 mmHg to keep the fracture reduced.

C. APPENDIX: MANUFACTURING STEPS FOR AN ARTIFICIAL ARM

Table 4. Manufacturing steps to produce the artificial arm

# No.	What/How/Description	Picture
1	Download forearm from GrabCAD library and convert the STL file into an SLDPRT file that can be altered in the CAD software program Solidworks	
2	In SolidWorks cut sweep a hole through the forearm with a diameter of 10.4 mm such that a straight steel rod can be placed in it. Split the forearm into individual pieces: a hand piece, a wrist piece and the length of the arm is split into four pieces with equal length.	
3	Add an inlet to each segment such that a silicone tube can be connected to it. Cut out holes so that the tubes from the front parts can run through all the parts. Add brims to attach the silicone bands that are made in steps 5 and 6	
4	From each segment make a mould such that silicone bands can be made with it for each piece. See steps . 3D print (<i>Original Prusa i3 MK3S+</i>) all the segments and corresponding mould parts.	
5	Mix equal parts A and B of <i>ecoflex™ 00-50</i> and pour it in the mould to create the first part of the silicone band	

# No.	What/How/Description	Picture
6	Place the mould with the silicone mixture in the vacuum degassing chamber to remove the gas bubbles from the mixture and let it cure for three hours.	
7	Repeat step 5 and 6 to create the second part of the silicone band. Leave the silicone band created in steps 5 and 6 on the segment such that the two silicone band parts are glued together during the cure time of the silicone.	
8	Glue cotton thread on the 3D printed segment such that silicone band made can be attached to the segment with <i>ecoflex</i> TM 00-50	
9	Degrease the 3D-printed part with soapy water and spray it with Plasti Dip aerosol. Let it dry for 20 min and apply a new layer. Repeat till four layers are applied and let it dry for four hours.	
10	Attach the silicone tubes to segments and assemble all individual segments back into the shape of a forearm on a straight steel rod	
11	Pour in the cavity of the forearm <i>ecoflex</i> TM 00-30 and let it set	

D. APPENDIX: SENSOR CALIBRATION

The pressure between the cast and the artificial arm is measured by thin film pressure sensors. Two different types (*SEN0295*, *DRFRobot*, *Shanghai, China* and *406 FSR*, *Interlink Electronics*, *Camarillo, California, USA*) will be tested and compared to each other to see which one has the better sensitivity range under the testing conditions of the smart memory (SM) cast. This is achieved by performing a compression test on the sensors and a foam sample with the same thickness as the foam layer in the cast. The sensors measure the voltage and time while the foam on top is compressed. The time, displacement and force are gathered from the compression machine. The sample rate of the sensors is 10 Hz. Due to the difference in the shape of the sensors, the *SEN0295* sensors will be referred to as the round sensors while the 406 FSR sensor will be called the square sensors from this point onward.

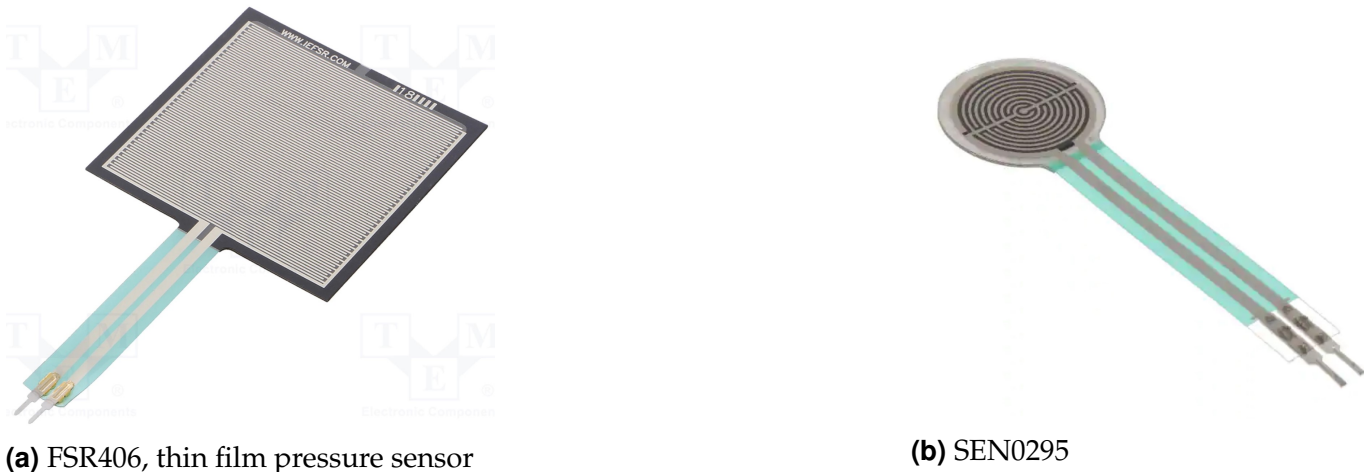
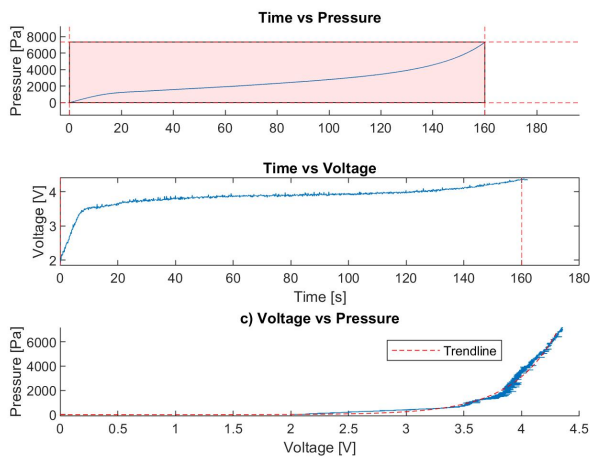


Fig. 17. The two thin film pressure sensors that were tested. [17a](#)) the FSR406 sensor has a active sensing area of 38.1 mm x 38.1 mm, while the SEN0295 has an active area with a diameter of 14.5 mm.

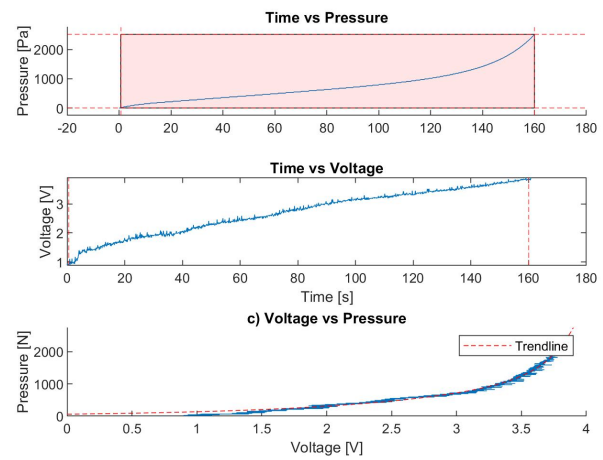
From the results of the compression test done to find a filler material, see appendix [A](#), and from the pressure measurements taken under a cast at Erasmus MC, appendix [B](#), it can be seen that pressure needed to maintain the reduction falls between the average plateau stress in PU40 foam and memory foam. Therefore, both these two materials will be tested with the sensors to see if the sensitivity of the sensor is influenced by it.

From the data obtained from the sensors, a time versus voltage plot is made such that the operating range of the sensor can be found in the testing conditions, as can be seen in the top figures of [18a](#) and [18b](#). Next, the corresponding period for the operating range is obtained from the time vs voltage plot from the middle plot in figures [18a](#) and [18b](#). Further, time versus force is plotted with the data from the compression test. The period related to the operating range in the sensors is then plotted on the time vs force plot to see which force range falls into the operating range of the sensors. The force range as well as the operating range are then plotted on the time vs force plot in a red square to visualize the operating range of the sensor. Lastly, the force measured by the compression machine is plotted against the voltage measured by the sensors. The strain rate of the compression test was 0.1 mm/s up until a strain of 80% of the foam layer. It was the same settings as in the compression tests performed on the different foam-type samples in appendix [A](#). This process is done for the two types of sensors.

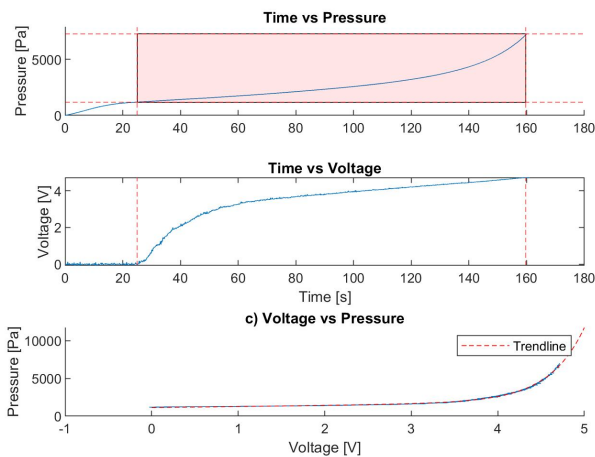
The operating range of the square sensors in combination with the memory foam decreases



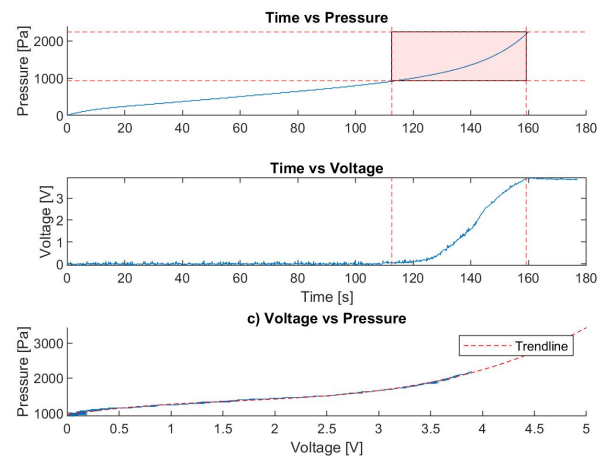
(a) Square sensor 1 with PU40 foam



(b) Square sensor 1 with MF foam



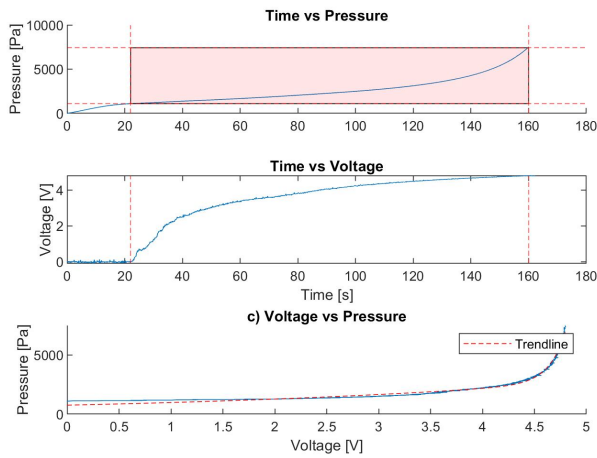
(c) Square sensor 2 with PU40 foam



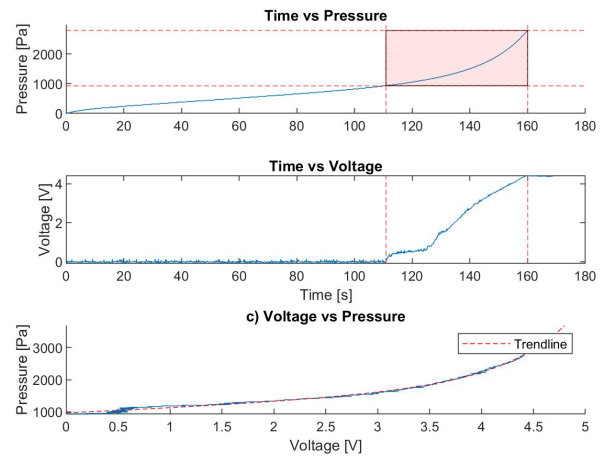
(d) Square sensor 2 with MF foam

Fig. 18. The data obtained from the compression test with square sensors 1, 2 and with 18a), 18c), PU40 foam and 18b), 18d), Memory foam. The vertical red stripe lines are the lines that indicate the period in which the sensors were actuated by the pressure applied to them during the compression test. The horizontal red-striped lines show the pressure range that corresponds with the period in which the sensor was actuated. The red box depicts the sensitivity range of the sensor. In the bottom plot, the voltage is plotted against the pressure such that the trend line can be found and used for converting the measured voltage into a pressure.

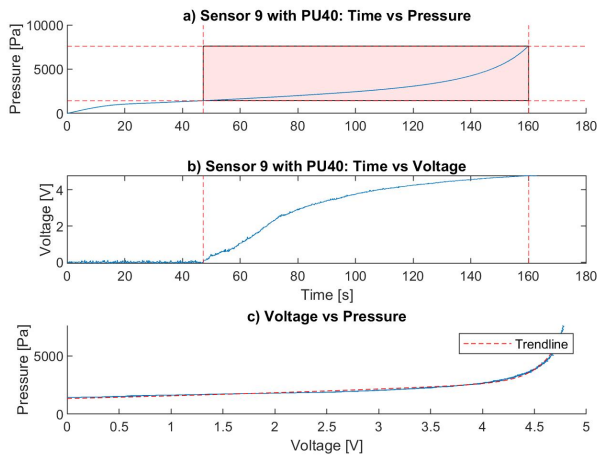
significantly, except in sensor 1, compared to when PU40 foam is used as can be seen in the figure 18. With memory foam, the sensor is only able to measure a force when the foam is in the densification phase. For the application of the SM cast, the sensor should at least be able to measure the force when the plateau phase is initiated since this is the effective range of the SM cast wherein the force does not increase as the foam is further compressed. When PU40 foam was placed on the sensor during the compression test it can be seen the sensors were able to sense the force in the early stages of the plateau phase or from the start of the compression test. From these results, it can be concluded that the square sensors in combination with memory foam as filler material would not be able to measure the pressure while the memory foam is compressed in the plateau phase. With PU40 on the



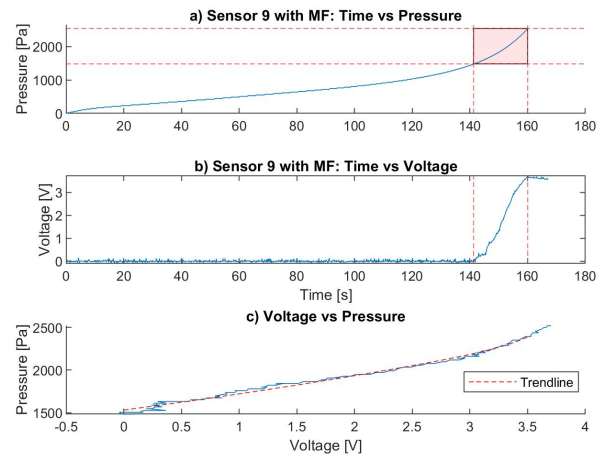
(e) Square sensor 3 with PU40 foam



(f) Square sensor 3 with MF foam



(g) Square sensor 4 with PU40 foam



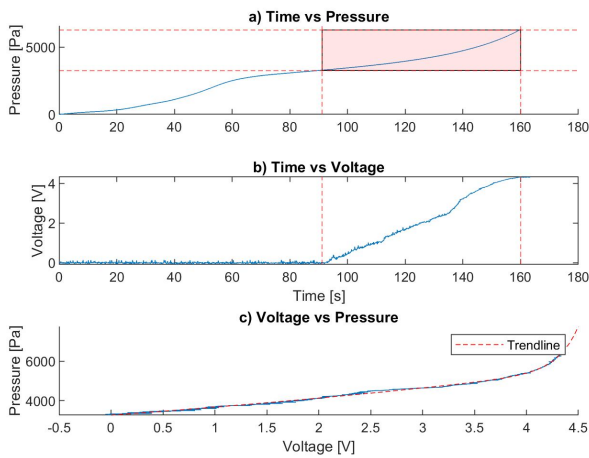
(h) Square sensor 4 with MF foam

Fig. 18. The data was obtained from the compression test with square sensor 3, 4 with 18e), 18g) PU40 foam and 18f), 18h) Memory foam. The vertical red stripe lines are the lines that indicate the period in which the sensors were actuated by the pressure applied to them during the compression test. The horizontal red-striped lines show the pressure range that corresponds with the period in which the sensor was actuated. The red box depicts the sensitivity range of the sensor. In the bottom plot, the voltage is plotted against the pressure such that the trend line can be found and used for converting the measured voltage into a pressure.

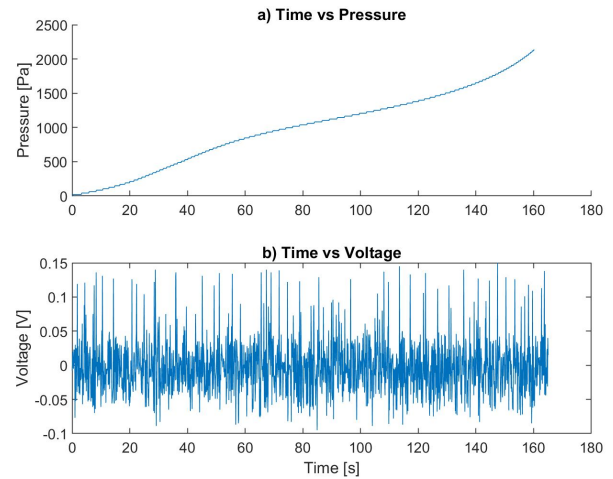
other hand, the operating range of the square sensors is large enough such that the plateau phase of the foam falls within this range. Therefore, the square sensors can be used in combination with PU40 foam.

Next, the round sensors were tested with PU40 and MF to obtain their sensitivity range. The results from these tests can be found in figure 19. The first four sensors were tested with PU40 and MF, however, as can be seen in figures 19a - 19h, some of the sensors were not able to pick up any signal while for others the sensitivity range had dropped significantly and did not provide any usable measurements. Therefore, from then on the sensors were only tested in combination with PU40 as

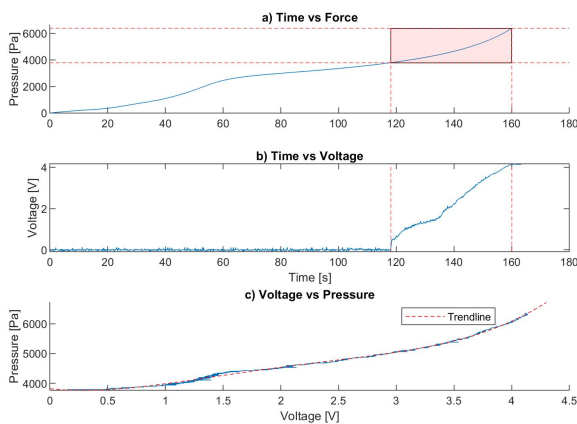
can be seen in figures 19i - 19o. The round sensor can thus not be used in combination with MF since the actuation force is located in the densification phase or the sensor is not actuated at all. PU40 foam combined with the round sensors gave divergent results regarding the sensitivity range. In sensors 1,2,4 and 6 the sensitivity range overlaps more with the densification phase of the foam, see figures 19a, 19c,19g and 19j. While for sensors 3, 5, 7 - 11 (19i,19k-19o) the sensitivity range increases and covers the plateau phase as well.



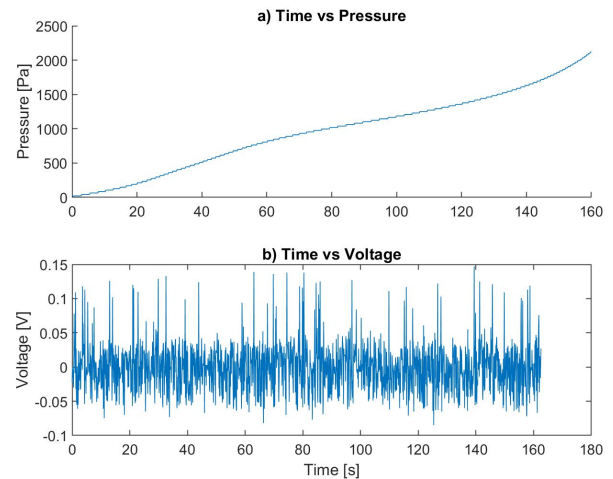
(a) Circle sensor 1 with PU40 foam



(b) Circle sensor 1 with MF foam



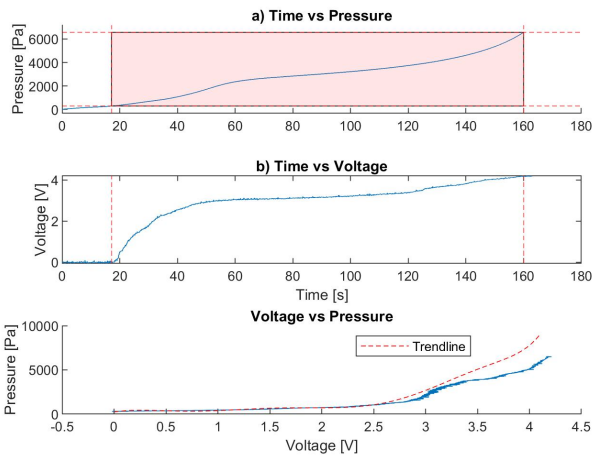
(c) Circle sensor 2 with PU40 foam



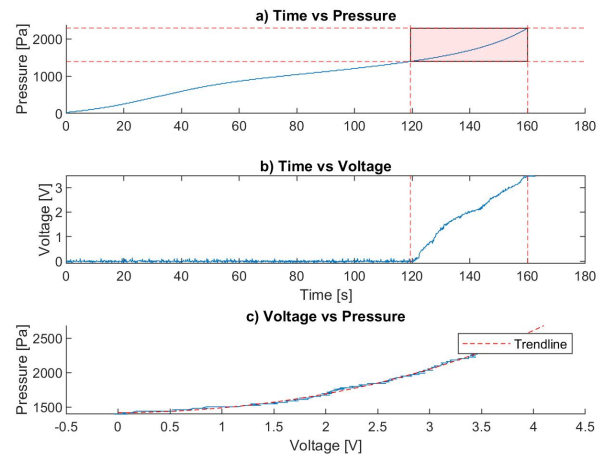
(d) Circle sensor 2 with MF foam

Fig. 19. The data obtained from the compression test with circle sensors 1 and 2 with 18a), 18c), PU40 foam and 18b), 18d), Memory foam. The vertical red stripe lines are the lines that indicate the period in which the sensors were actuated by the pressure applied to them during the compression test. The horizontal red-striped lines show the pressure range that corresponds with the period in which the sensor was actuated. The red box depicts the sensitivity range of the sensor. In the bottom plot, the voltage is plotted against the pressure such that the trend line can be found and used for converting the measured voltage into a pressure.

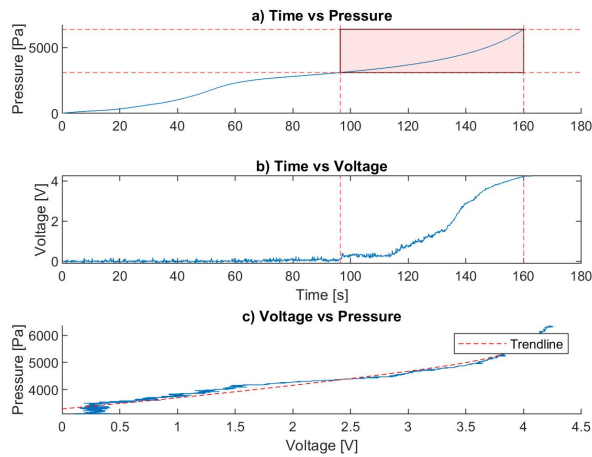
To map the voltage readings from the sensors with the stress from the compression test a lookup table was made for the sensors in Matlab. These results can be found in 20



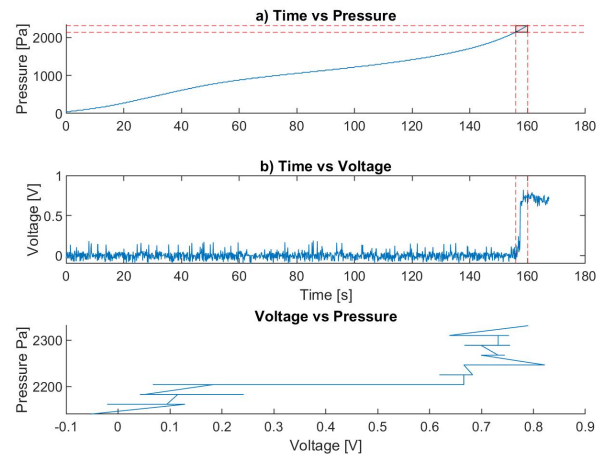
(e) Circle sensor 3 with PU40 foam



(f) Circle sensor 3 with MF foam



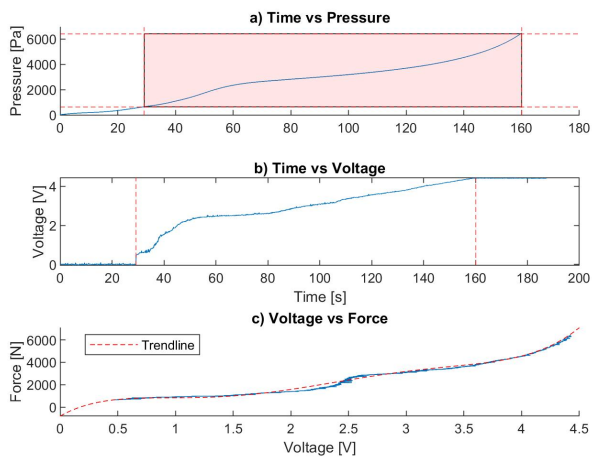
(g) Circle sensor 4 with PU40 foam



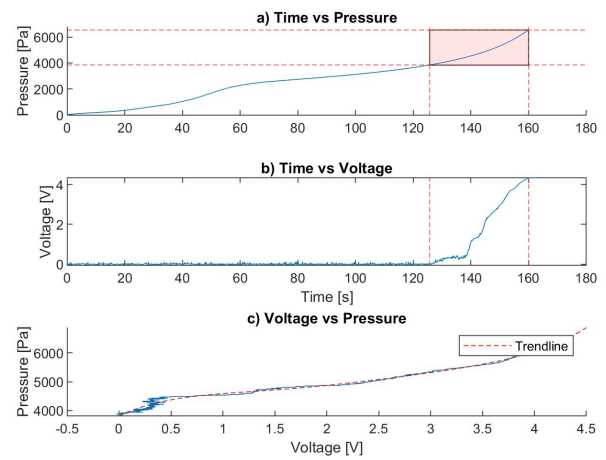
(h) Circle sensor 4 with MF

Fig. 19. The data obtained from the compression test with circle sensors 3 and 4 with 19e), 19g) PU40 foam and 19f), 19h) Memory foam. The vertical red stripe lines are the lines that indicate the period in which the sensors were actuated by the pressure applied to them during the compression test. The horizontal red-striped lines show the pressure range that corresponds with the period in which the sensor was actuated. The red box depicts the sensitivity range of the sensor. In the bottom plot, the voltage is plotted against the pressure such that the trend line can be found and used for converting the measured voltage into a pressure.

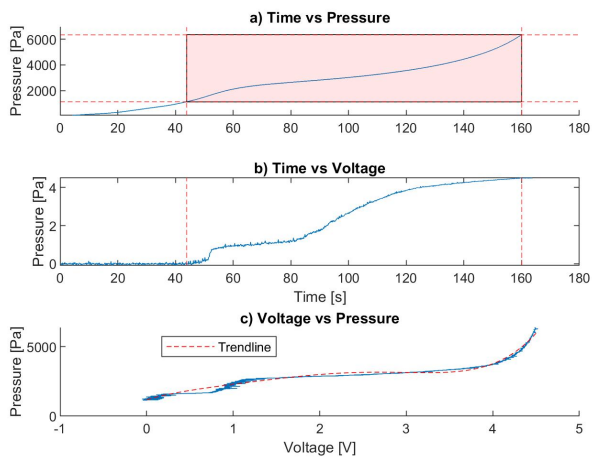
Next, the round sensors were tested with PU40 and MF to obtain their sensitivity range. The results from these tests can be found in figure 19. The first four sensors were tested with PU40 and MF, however, as can be seen in figures 19a - 19h, some of the sensors were not able to pick up any signal while for others the sensitivity range had dropped significantly and did not provide any usable measurements. Therefore, from then on the sensors were only tested in combination with PU40 as can be seen in figures 19i - 19o. The round sensor can thus not be used in combination with MF since the actuation force is located in the densification phase or the sensor is not actuated at all. PU40 foam combined with the round sensors gave divergent results regarding the sensitivity range. In sensors 1,2,4 and 6 the sensitivity range overlaps more with the densification phase of the foam, see figures



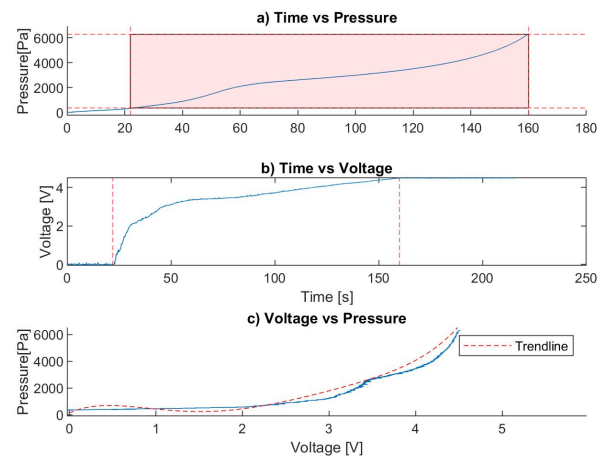
(i) Circle sensor 5 with PU40 foam



(j) Circle sensor 6 with PU40 foam



(k) Circle sensor 7 with PU40 foam

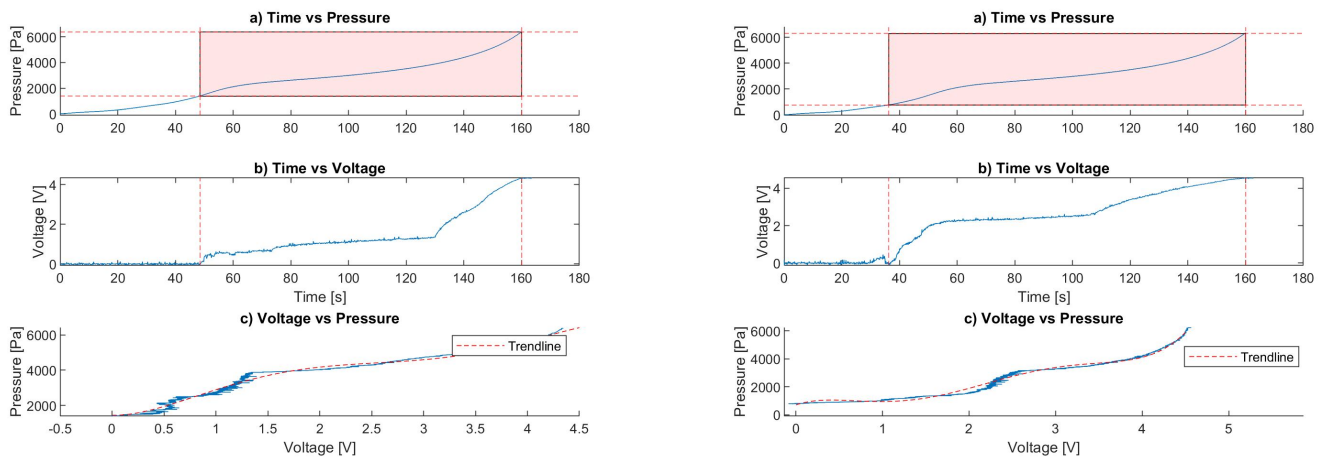


(l) Circle sensor 8 with PU40 foam

Fig. 19. The data obtained from the compression test with circle sensor and sensor 5 - 8 with PU40 foam (19i - 19l). The vertical red stripe lines are the lines that indicate the period in which the sensors were actuated by the pressure applied to them during the compression test. The horizontal red-striped lines show the pressure range that corresponds with the period in which the sensor was actuated. The red box depicts the sensitivity range of the sensor. In the bottom plot, the voltage is plotted against the pressure such that the trend line can be found and used for converting the measured voltage into a pressure.

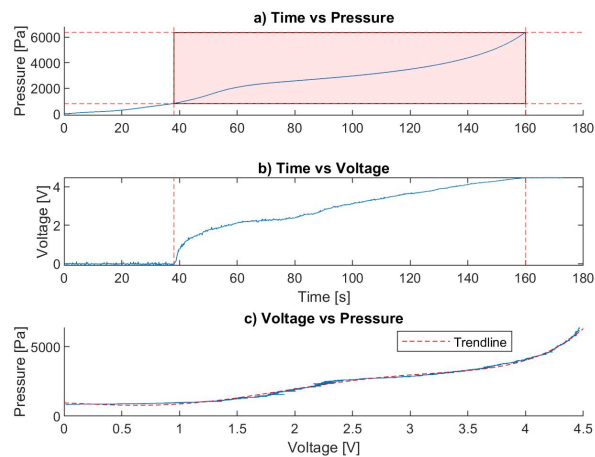
19a, 19c, 19g and 19j. While for sensors 3, 5, 7 - 11 (19i, 19k-19o) the sensitivity range increases and covers the plateau phase as well.

The sensitivity range for the square and round sensors in combination with PU40 is similar as can be seen in figures 18 and 19e, 19i and 19k-19o. Further, it was decided to only inflate the hand, wrist and first part of the artificial arm since these are in the proximity of the location of a DRF in a patient. So, only three parts will be inflated instead of the original six parts. Due to the smaller size of the circle sensors and that there were six sensors that were calibrated, it was opted to use those.



(m) Circle sensor 9 with PU40 foam

(n) Circle sensor 10 with PU40



(o) Circle sensor 11 with PU40 foam

Fig. 19. The data was obtained from the compression test with circle sensor 9 - 11 (19m-19o) and PU40 foam. The vertical red stripe lines are the lines that indicate the period in which the sensors were actuated by the pressure applied to them during the compression test. The horizontal red-striped lines show the pressure range that corresponds with the period in which the sensor was actuated. The red box depicts the sensitivity range of the sensor. In the bottom plot, the voltage is plotted against the pressure such that the trendline can be found and used for converting the measured voltage into a pressure.

E. APPENDIX: RESULTS OF EXPERIMENTS

In this appendix, more results can be found of the different experiments performed, see figures 21, 22 and 23. Experiments where only one of the two sensors picked up a signal were not added. A hysteresis test was also performed on the wrist segment in the SMC and TC and these results can be found in 24. The sensors placed on the hand segment were sensor 8 on the top side and sensor 11 on the bottom side. On the wrist. Part I in this appendix corresponds with the forearm segment in the paper. Sensor 5 is placed on the top of this segment and sensor 7 on the bottom side.

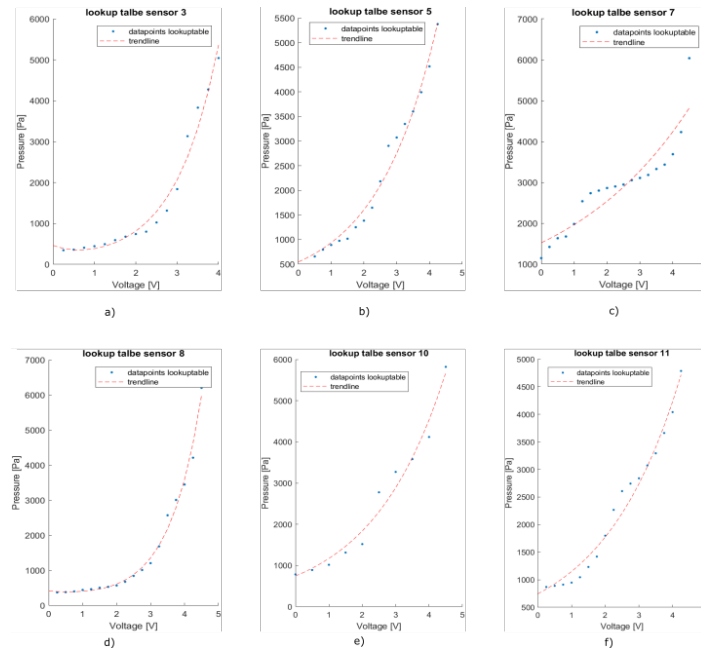


Fig. 20. Results from the lookup table for sensors that are used during the experiments with the SMC and TC.

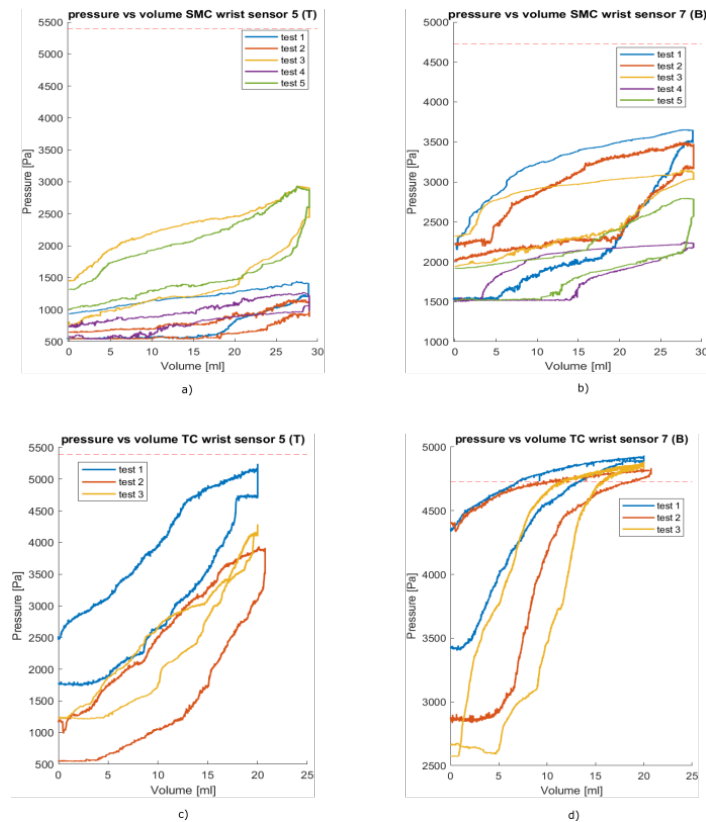


Fig. 21. Results from testing the wrist in the SMC and TC.

F. APPENDIX: FILE MANUAL

In this appendix, a description is giving on how the files are organized that are handed in at the end of this thesis project. These are the files and data from the experiments that were used to

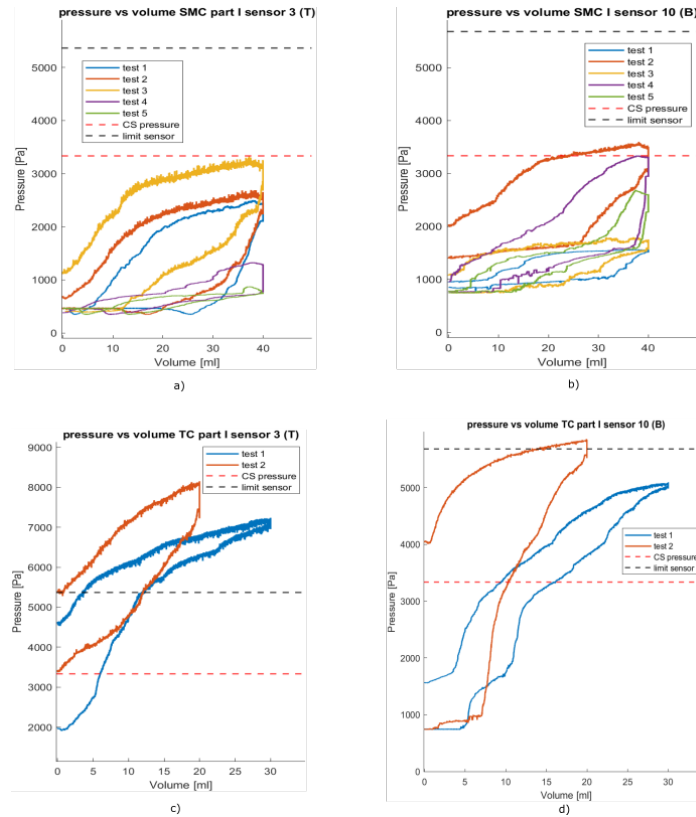


Fig. 22. Results from testing forearm in the SMC and TC.

complete the project. There are 4 main folders: compression test, artificial arm, sensor calibration and results. In the compression test folder, all the results from the compression test performed at UvA are placed. Further, Matlab files to plot the stress-strain curves are in there as well. All the files needed to manufacture the artificial arm and the corresponding moulds for the silicone bands are in the artificial arm folder. They are further categorised by each segment individually. In the sensor calibration folder, the data from the compression test and the sensors during the compression test are stored. The Matlab files with the calibration for each sensor is also stored in there. In the final folder of the results, all the data from the experiments with the SMC and the TC can be found as well as the Matlab files.

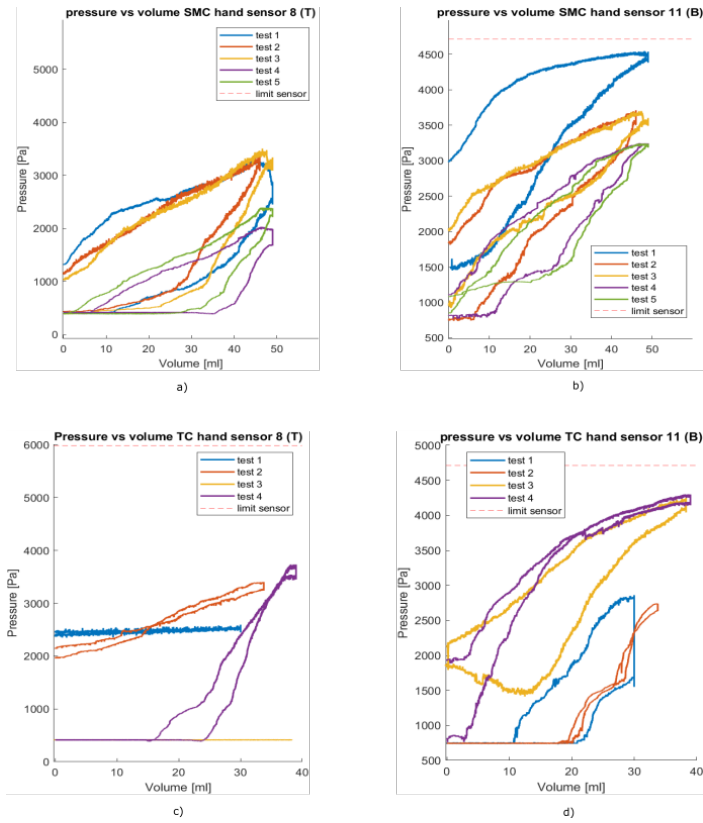


Fig. 23. Results from testing the hand in the SMC and TC.

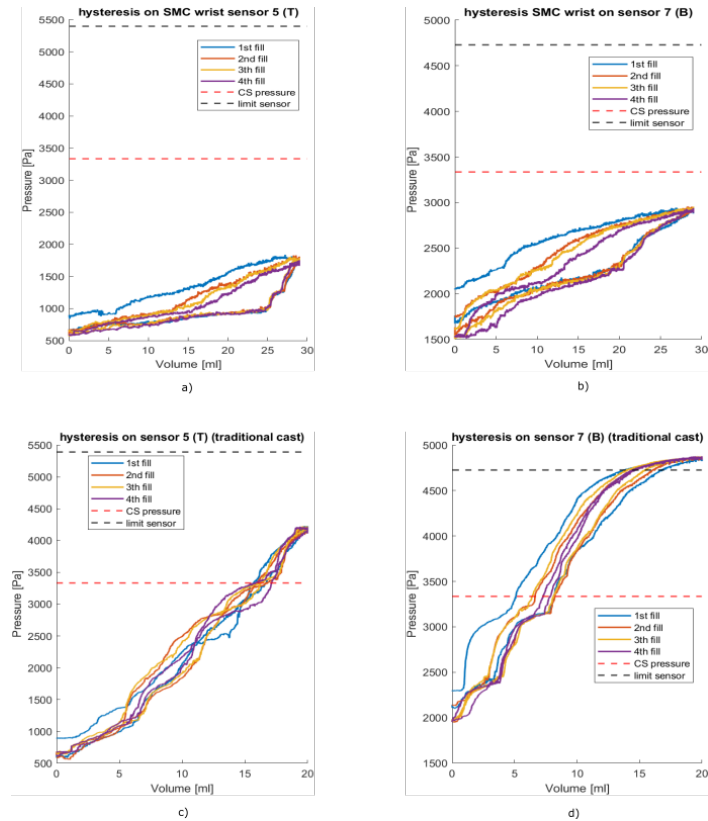


Fig. 24. Hysteresis test performed with the wrist part in the SMC and TC